

New asteroseismic rotation rates of *Kepler* dwarfs show strong agreement with weakened magnetic braking on the late-age main sequence

Oliver J. Hall^{1,2,3,*}, Guy R. Davies^{2,3}, Jennifer van Saders^{4,5,6}, Martin B. Nielsen^{2,3}, Mikkel N. Lund³, William J. Chaplin^{2,3}, Rafael A. García^{7,8}, Louis Amard⁹, Angela A. Breimann⁹, Saniya Khan^{2,3}, Victor See⁹, Jamie Tayar^{4,10}

¹ European Space Agency (ESA), European Space Research and Technology Centre (ESTEC), Keplerlaan 1, 2201 AZ Noordwijk, The Netherlands

² School of Physics and Astronomy, University of Birmingham, Edgbaston, Birmingham, B15 2TT, UK

³ Stellar Astrophysics Centre, Department of Physics and Astronomy, Aarhus University, Ny Munkegade 120, 8000 Aarhus C, Denmark

⁴ Institute for Astronomy, University of Hawai'i, Honolulu, HI 96822

⁵ Observatories of the Carnegie Institution for Science, Pasadena, CA 91101

⁶ Department of Astrophysical Sciences, Princeton University, Princeton, NJ 08544

⁷ IRFU, CEA, Université Paris-Saclay, F-91191 Gif-sur-Yvette, France

⁸ AIM, CEA, CNRS, Université Paris-Saclay, Université Paris Diderot, Sorbonne Paris Cité, F-91191 Gif-sur-Yvette, France

⁹ University of Exeter Department of Physics and Astronomy, Stocker Road, Devon, Exeter, EX4 4QL, UK

¹⁰ Hubble Fellow

Studies using asteroseismic ages and rotation rates from star spot rotation have shown that standard age-rotation relations break down roughly half-way through the main sequence lifetime, a phenomenon referred to as weakened magnetic braking. While rotation rates from spots can be difficult to determine for older, less active stars, rotational splitting of asteroseismic oscillation frequencies can provide rotation rates for both active and quiescent stars, and so can confirm whether this effect really takes place in older stars.

We obtained asteroseismic rotation rates of 91 main sequence stars showing high signal-to-noise modes of oscillation. Using these new rotation rates, along with effective temperatures, metallicities and seismic masses and ages, we built a hierarchical Bayesian mixture model to determine whether the ensemble more closely agreed with a standard rotational evolution scenario [1], or one where weakened magnetic braking takes place [2]. The weakened magnetic braking scenario was found to be 98.4% more likely for our stellar ensemble, adding to the growing body of evidence for this stage of stellar rotational evolution. This work represents the largest catalogue of seismic rotation on the main sequence to date, opening up possibilities for more detailed ensemble analysis of rotational evolution with *Kepler*.

*Email: oliver.hall@esa.int — Twitter: @astronomer — GitHub: @ojhall194

Gyrochronology is the study of the relationship between a star’s rotation period and its age. As a star grows older along the main sequence, magnetic winds will cause it to lose angular momentum, slowing it down. Because the loss rate is related to temperature, the rotation period of a young star will rapidly settle on to a plane in age-colour-rotation space [3]. As a result, knowing the rotation and colour of a star provides an avenue to measure its age, which can otherwise be difficult to come by, enabling more in-depth studies of stellar populations and individual stars [4, 5].

Gyrochronology was previously calibrated on stellar clusters, which have well constrained ages, but only up to roughly 2.5 Gyr so far [6]. With the launch of the *Kepler* mission [7], ages of main sequence field stars (i.e. not in clusters) became more widely available through asteroseismology, the study of stellar variability [8]. When looking at these stars, disagreements were found with gyrochronology beyond the middle of their main sequence lifetime, which could not be reconciled with existing theories [9, 10, 11]. It was proposed that at some stage in a star’s evolution it undergoes *weakened magnetic braking* (WMB, [2]), where the efficiency of angular momentum loss rapidly drops, causing stars to keep fast rotation rates at old ages, which we would not expect from existing gyrochronology relations.

The mechanism by which weakened magnetic braking occurs is still subject to debate, and may be connected to changes in the magnetic field morphology [12, 13, 14, 15]. It may also be explained from an observational point of view. A large scale survey of stellar rotation rates measured using star spots pointed out a lack of slowly rotating stars older than Sun [16]. As activity reduces with age, older stars with fewer star spots are less likely to have their rotation measured [17]. The point at which the detection probability drops appears to lie at a similar level of activity to that at which the proposed weakened magnetic braking takes place, pitting these two possibilities against one another [18].

Determining whether weakened magnetic braking is a true phenomenon or a bias in star spot observations requires new data, which can be provided by asteroseismology. A star’s rotation causes modes of oscillation to split into multiplets, making it possible to measure the rate of rotation by measuring the splitting between oscillation frequencies [19]. Asteroseismic rotation is more difficult to obtain than rotation from star spots, but does not require spots to be visible, meaning that we can measure rotation for quiescent stars that would not have been present in existing catalogues of star-spot rotation. Previous studies have shown that asteroseismic rotation rates probe the near-surface of the star, making them comparable to spot rotation rates, and the perfect avenue to explore whether weakened magnetic braking truly takes place [20, 21]. Here, we measured asteroseismic rotation rates of 91 main sequence stars across a broad range of colours and ages, and evaluate this new ensemble to determine whether it agrees more closely with a classical rotational evolution scenario, or one where weakened magnetic braking takes place.

Asteroseismic main sequence targets: In order to obtain robust asteroseismic rotation rates, we required detections of multiples of both dipole (denoted as $\ell = 1$) and quadrupole ($\ell = 2$) oscillations for each star, of which the latter have significantly lower signal-to noise. Radial oscillations ($\ell = 0$), which are also visible, do not split. In this work, we studied a sample of 95 of the highest signal-to-noise targets observed by *Kepler*, combining the ‘Kages’

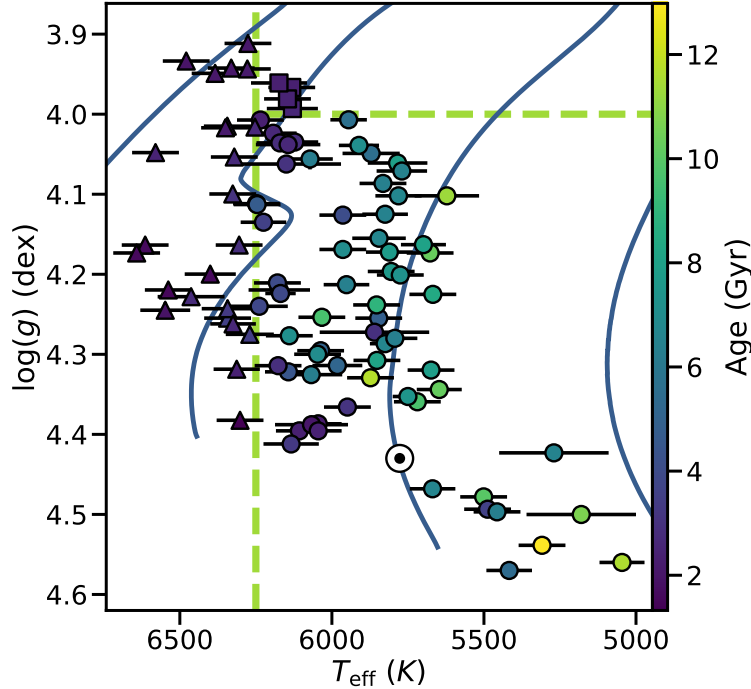


Figure 1: Our sample of 95 stars from the Kages and LEGACY catalogues coloured by asteroseismic age [8, 24]. The dashed lines indicate our classification boundaries: main sequence (circles, $T_{\text{eff}} < 6250 \text{ K}$, $\log(g) < 4 \text{ dex}$), potential sub-giants (squares, $T_{\text{eff}} < 6250 \text{ K}$, $\log(g) > 4 \text{ dex}$), and ‘hot’ stars (triangles, $T_{\text{eff}} > 6250 \text{ K}$). The Sun is shown with the ‘ \odot ’ symbol, and has an age of 4.6 Gyr [28]. The solid lines are evolutionary tracks generated using MESA [29], for a metallicity of $Z = 0.01493$ and helium content of $Y = 0.26588$. Left to right, they represent masses of 1.5 , 1.25 , 1 and $0.75 M_{\odot}$. Vertical errorbars are too small to be visible.

[8, 22] and LEGACY [23, 24] catalogues*. A table of parameters taken from these studies, as well as details on how these were obtained, can be found in **Methods**.

We separated our sample into three categories [25]: 64 main sequence stars (MS, $\log(g) > 4.0 \text{ dex}$, $T_{\text{eff}} < 6250 \text{ K}$); 4 potential sub-giant stars (SG, $\log(g) < 4.0 \text{ dex}$, $T_{\text{eff}} < 6250 \text{ K}$, which may have begun to evolve off the main sequence, complicating their rotational history[†]; and 24 ‘hot’ stars (H, $T_{\text{eff}} > 6250 \text{ K}$), which lie above the Kraft break, the point at which convective envelopes are tenuous, and angular momentum loss through magnetic winds becomes inefficient [27]. Our conclusions are largely insensitive to these categorical assignments, and they are intended solely to help explore results category-by-category. The sample, which can be seen in Figure 1, spans surface gravities of $3.8 \text{ dex} < \log(g) < 4.6 \text{ dex}$, temperatures of $5000 \text{ K} < T_{\text{eff}} < 6700 \text{ K}$, and ages from 1 to $\sim 13 \text{ Gyr}$.

Results of asteroseismic fitting: The ‘Kages’ and LEGACY catalogues that form our

*For these catalogues the mode extraction through frequency fitting [22, 23] and modelling using mode frequencies to obtain stellar parameters [8, 24] are covered in separate papers.

[†]It should be noted that none of these stars have identified mixed dipole modes, which indicate an evolved structure (see [26]).

stellar sample both performed detailed asteroseismic frequency fitting, but did not report asteroseismic rotation. Here, we repeated the mode frequency fitting with an improved Bayesian model that accounted for rotation in more detail (see **Methods**). We fit our model to *Kepler* power-spectra of 95 stars, which was successful in 94 cases. We compared our results with both published and unpublished asteroseismic rotation rates, and found that the three stars with the lowest angles of inclination ($< 10^\circ$) were inconsistent with previous work. To some degree this was expected, as for stars viewed near pole-on the power of the split modes of oscillation are extremely small. We flagged our rotation rates for these stars, and did not use them in the next steps in our analysis, leaving a sample of 91 stars for which we judge our asteroseismic rotation measurements to be robust (for a full justification, see **Methods**).

Seismic versus surface rotation rates:

Comparing gyrochronology models: To evaluate the implications of our seismic ensemble for gyrochronology, we compared our new asteroseismic rotation rates to two models of rotational evolution: a ‘standard’ model, which assumes a traditional angular momentum transport through magnetically driven stellar winds [30, 31], and one where weakened magnetic braking takes place (hereafter the ‘WMB model’). The WMB model was identical to the standard model in its input physics, except for the condition that angular momentum loss ceases above a critical Rossby number of $Ro_{\text{crit}} = 1.97$ (for details, see **Methods**).

We evaluated our ensemble against both population models simultaneously using a Bayesian mixture model, which treated the data as being drawn from a mixture made from Kernel Density Estimates of both populations, modulated by a mixing parameter P_s . In the limit that $P_s \rightarrow 1$, the data are mostly likely drawn from the standard model. In the limit $P_s \rightarrow 0$, the WMB model is more likely. This mixture model was evaluated in a five-dimensional parameter space, accounting for the population distributions in effective temperature (T_{eff}), metallicity ($[\text{Fe}/\text{H}]$), asteroseismic mass (M) and age (t) and our new rotation periods (P).

We fit our mixture model to the 73 stars in our sample with the best convergence metrics on the asteroseismic mode frequency fitting (see **Table 1**). This sample included 22 ‘hot’ stars, 4 potential sub-giants, and 47 main sequence stars. We calculated a joint posterior for this sample by multiplying the posterior probabilities obtained for P_s for each stars. This joint probability can be seen in Figure 2 in the left-hand plot, and the cumulative probability can be seen in the right-hand plot. In both of these plots, their left-hand sides hold 98.4% of the probability, indicating that the weakened magnetic braking model is preferred. When only considering the main sequence stars, which are expected to be driving this distinction, this rises to 99.2%.

Verifying consequences for gyrochronology: In order to verify that our results presented a meaningful confirmation of weakened magnetic braking, we made sure to test the same results were obtained using different subsets of the ensemble. Figure 3 shows [metallicity, full sample, biases, asteroseismology, van saders].

We leave the reader with the following conclusions:

1. We found that our ensemble was 98.4% more likely to be drawn from the WMB model than the standard model, for stars evolved under a standard braking law [1]. In other

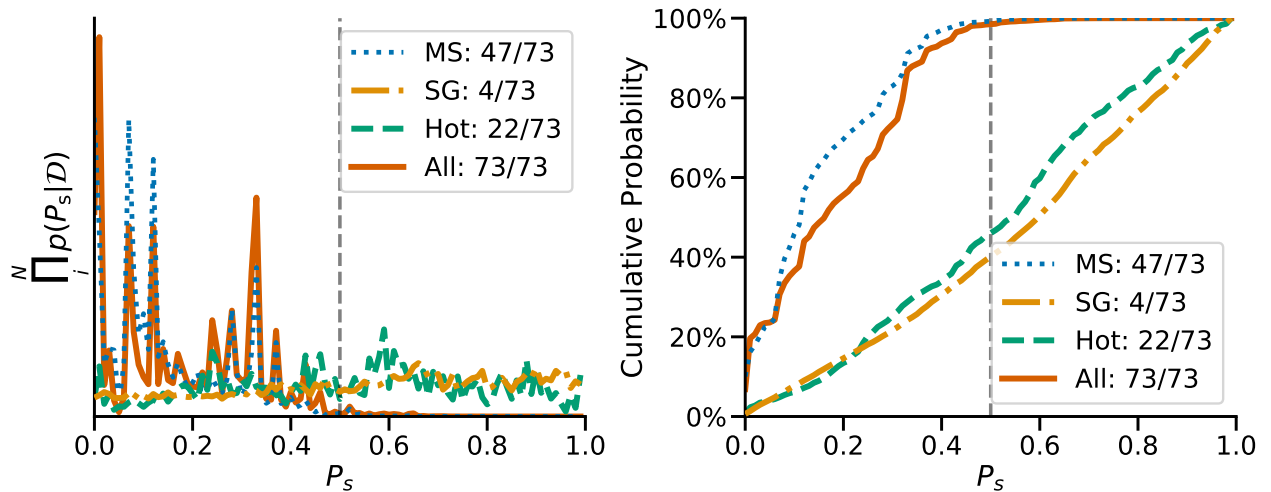


Figure 2: Posterior estimates of the mixture model parameter P_s , broken down by stellar classification. A value of P_s close to zero indicates that the data are more consistent with a rotational evolution that includes weakened magnetic braking, whereas a value close to 1 indicates that the data are more consistent with a standard rotational evolution scenario. *Left*: the product of histograms of the posterior estimates for 73 stars, or subsets thereof for different stellar classifications. *Right*: the cumulative posterior probability for 73 stars, or subsets thereof for different stellar types.

words, our asteroseismic observations strongly favour a model of weakened magnetic braking [2], at a critical Rossby number of $Ro_{\text{crit}} = 1.97$. This work expands upon previous analysis ([18]) by including quiescent stars older than the Sun. This conclusion was found to be robust against choice of ensemble members and potentially underestimated asteroseismic systematic uncertainties. A comparison to other braking laws [17] using our asteroseismic ensemble will take place in future work.

2. We compared our new asteroseismic rotation rates with surface rotation measures from spot modulation. Our findings replicate those in similar studies ([10, 21]), in the sense that we find no statistically significant difference between seismic and spot modulation measures of stellar rotation in our ensemble.
3. We present new techniques for asteroseismic ‘peak-bagging’ frequency analyses, specifically: expressing well known empirical asteroseismic relations in a hierarchical modeling structure to account for small-scale effects not included in our model (such as acoustic glitches), and replacing uninformative empirical relations with Gaussian Process priors.
4. The new asteroseismic rotation catalogue presented in this work will act as an entry point for more detailed studies, including comparisons between different braking laws and individually modeled values of stellar rotation at different critical Rossby numbers.

Finally, in the near future our asteroseismic rotation catalogue will be further complemented; with high-precision surface rotation measurements and atmospheric parameters from spectroscopic surveys such as LAMOST [32], 4MOST [33] and WEAVE [34]; and new asteroseismic measurements of age from the K2 and *TESS* missions. With these surveys, large

scale ensemble asteroseismology will continue to increase the possibilities for understanding gyrochronology.

All analysis performed as part of this work is stored in an online public repository[‡].

Software: `astropy` [35, 36], `astroquery` [37], `Lightkurve` [38], `corner` [39], `emcee` [40], `daft`, `Stan` [41], `PyStan` [42], `iPython` [43], `Jupyter Notebooks` [44], `numpy` [45], `pandas` and `scipy` [46], `matplotlib` [47], `seaborn` [48], `statsmodels` [49], `PyMC3` [50], `theano` [51].

Acknowledgments: The authors would like to thank Sean Matt, Ellis Avallone, Alex Dixon, Warrick Ball and Brett Morris for helpful discussions. OJH, GRD and WJC acknowledge the support of the UK Science and Technology Facilities Council (STFC). JvS acknowledges support from the TESS Guest Investigator Program (80NSSC18K18584). MBN acknowledges support from the UK Space Agency This work has received funding from the European Research Council (ERC) under the European Union’s Horizon 2020 research and innovation programme (CartographY GA. 804752) Funding for the Stellar Astrophysics Centre is provided by The Danish National Research Foundation (Grant agreement no.: DNRF106). LA, AB and VS acknowledge funding from the European Research Council (ERC) under the European Union’s Horizon 2020 research and innovation program (grant agreement No. 682393 AWESoMeStars). AB also acknowledges the support of the College of Engineering, Mathematics and Physical Sciences at the University of Exeter. RAG acknowledges the support from the PLATO and GOLF CNES grants. JT acknowledges that support for this work was provided by NASA through the NASA Hubble Fellowship grant #51424 awarded by the Space Telescope Science Institute, which is operated by the Association of Universities for Research in Astronomy, Inc., for NASA, under contract NAS5-26555. The computations described in this paper were performed using the University of Birmingham’s BlueBEAR HPC service. This paper includes data collected by the Kepler mission and obtained from the MAST data archive at the Space Telescope Science Institute (STScI). Funding for the Kepler mission is provided by the NASA Science Mission Directorate. STScI is operated by the Association of Universities for Research in Astronomy, Inc., under NASA contract NAS 5–26555.

References

- [1] van Saders, J. L. & Pinsonneault, M. H. Fast Star, Slow Star; Old Star, Young Star: Subgiant Rotation as a Population and Stellar Physics Diagnostic. *The Astrophysical Journal* **776**, 67 (2013).
- [2] van Saders, J. L. *et al.* Weakened magnetic braking as the origin of anomalously rapid rotation in old field stars. *Nature* **529**, 181 (2016).
- [3] Barnes, S. A. Ages for Illustrative Field Stars Using Gyrochronology: Viability, Limitations, and Errors. *The Astrophysical Journal* **669**, 1167 (2007).

[‡]<https://github.com/ojhall94/malatium>

- [4] Leiner, E., Mathieu, R. D., Vanderburg, A., Gosnell, N. M. & Smith, J. C. Blue Lurkers: Hidden Blue Stragglers on the M67 Main Sequence Identified from Their Kepler/K2 Rotation Periods. *The Astrophysical Journal* **881**, 47 (2019).
- [5] Claytor, Z. R. *et al.* Chemical Evolution in the Milky Way: Rotation-based ages for APOGEE-Kepler cool dwarf stars. *arXiv e-prints* arXiv:1911.04518 (2019).
- [6] Meibom, S. *et al.* A spin-down clock for cool stars from observations of a 2.5-billion-year-old cluster. *Nature* **517**, 589 (2015).
- [7] Borucki, W. J., Koch, D. & Team, K. S. Kepler Planet Detection Mission: Highlights of the First Results. *AAS/Division for Planetary Sciences Meeting Abstracts #42* **42**, 47.03 (2010).
- [8] Silva Aguirre, V. *et al.* Ages and fundamental properties of Kepler exoplanet host stars from asteroseismology. *Monthly Notices of the Royal Astronomical Society* **452**, 2127 (2015).
- [9] Angus, R., Aigrain, S., Foreman-Mackey, D. & McQuillan, A. Calibrating gyrochronology using Kepler asteroseismic targets. *Monthly Notices of the Royal Astronomical Society* **450**, 1787 (2015).
- [10] Nielsen, M. B., Schunker, H., Gizon, L. & Ball, W. H. Constraining differential rotation of Sun-like stars from asteroseismic and starspot rotation periods. *Astronomy and Astrophysics* **582**, A10 (2015).
- [11] Davies, G. R. *et al.* Asteroseismic inference on rotation, gyrochronology and planetary system dynamics of 16 Cygni. *Monthly Notices of the Royal Astronomical Society* **446**, 2959 (2015).
- [12] Réville, V., Brun, A. S., Matt, S., Strugarek, A. & Pinto, R. The effect of magnetic topology on thermally-driven winds: Towards a general formulation of the braking law. *The Astrophysical Journal* **798**, 116 (2015). 1410.8746.
- [13] Garraffo, C., Drake, J. J. & Cohen, O. The Missing Magnetic Morphology Term in Stellar Rotation Evolution. *Astronomy & Astrophysics* **595**, A110 (2016). 1607.06096.
- [14] Metcalfe, T. S. *et al.* LBT/PEPSI Spectropolarimetry of a Magnetic Morphology Shift in Old Solar-type Stars. *arXiv:1912.01186 [astro-ph]* (2019). 1912.01186.
- [15] See, V. *et al.* Do Non-dipolar Magnetic Fields Contribute to Spin-down Torques? *The Astrophysical Journal* **886**, 120 (2019).
- [16] McQuillan, A., Mazeh, T. & Aigrain, S. Rotation Periods of 34,030 Kepler Main-Sequence Stars: The Full Autocorrelation Sample. *The Astrophysical Journal Supplement Series* **211**, 24 (2014). 1402.5694.
- [17] Matt, S. P., Brun, A. S., Baraffe, I., Bouvier, J. & Chabrier, G. The Mass-dependence of Angular Momentum Evolution in Sun-like Stars. *The Astrophysical Journal* **799**, L23 (2015).

- [18] van Saders, J. L., Pinsonneault, M. H. & Barbieri, M. Forward Modeling of the Kepler Stellar Rotation Period Distribution: Interpreting Periods from Mixed and Biased Stellar Populations. *The Astrophysical Journal* **872**, 128 (2019).
- [19] Ledoux, P. The Nonradial Oscillations of Gaseous Stars and the Problem of Beta Canis Majoris. *The Astrophysical Journal* **114**, 373 (1951).
- [20] Lund, M. N., Miesch, M. S. & Christensen-Dalsgaard, J. Differential rotation in main-sequence solar-like stars: Qualitative inference from asteroseismic data. *The Astrophysical Journal* **790**, 121 (2014). 1406.7873.
- [21] Benomar, O., Takata, M., Shibahashi, H., Ceillier, T. & García, R. A. Nearly uniform internal rotation of solar-like main-sequence stars revealed by space-based asteroseismology and spectroscopic measurements. *Monthly Notices of the Royal Astronomical Society* **452**, 2654–2674 (2015).
- [22] Davies, G. R. *et al.* Oscillation frequencies for 35 Kepler solar-type planet-hosting stars using Bayesian techniques and machine learning. *Monthly Notices of the Royal Astronomical Society* **456**, 2183 (2016).
- [23] Lund, M. N. *et al.* Standing on the Shoulders of Dwarfs: The Kepler Asteroseismic LEGACY Sample. I. Oscillation Mode Parameters. *The Astrophysical Journal* **835**, 172 (2017).
- [24] Silva Aguirre, V. *et al.* Standing on the Shoulders of Dwarfs: The Kepler Asteroseismic LEGACY Sample. II. Radii, Masses, and Ages. *The Astrophysical Journal* **835**, 173 (2017).
- [25] García, R. A. *et al.* Rotation and magnetism of Kepler pulsating solar-like stars. Towards asteroseismically calibrated age-rotation relations. *Astronomy and Astrophysics* **572**, A34 (2014).
- [26] Bedding, T. R. *et al.* Solar-like Oscillations in Low-luminosity Red Giants: First Results from Kepler. *The Astrophysical Journal Letters* **713**, L176–L181 (2010).
- [27] Kraft, R. P. Studies of Stellar Rotation. V. The Dependence of Rotation on Age among Solar-Type Stars. *The Astrophysical Journal* **150**, 551 (1967).
- [28] Bonanno, A. & Fröhlich, H.-E. A Bayesian estimation of the helioseismic solar age. *Astronomy and Astrophysics* **580**, A130 (2015).
- [29] Paxton, B. *et al.* Modules for Experiments in Stellar Astrophysics (MESA): Convective Boundaries, Element Diffusion, and Massive Star Explosions. *arXiv:1710.08424 [astro-ph]* (2017). 1710.08424.
- [30] Skumanich, A. TIME SCALES FOR Ca II EMISSION DECAY, ROTATIONAL BRAKING, AND LITHIUM DEPLETION. *ApJ*. . . 4 (1972).
- [31] Kawaler, S. D. Angular momentum loss in low-mass stars. *The Astrophysical Journal* **333**, 236 (1988).

- [32] Deng, L.-C. *et al.* LAMOST Experiment for Galactic Understanding and Exploration (LEGUE) — The survey’s science plan. *Research in Astronomy and Astrophysics* **12**, 735–754 (2012).
- [33] de Jong, R. S. *et al.* 4MOST: 4-metre Multi-Object Spectroscopic Telescope **9147**, 91470M (2014).
- [34] Dalton, G. *et al.* Project overview and update on WEAVE: The next generation wide-field spectroscopy facility for the William Herschel Telescope **9147**, 91470L (2014).
- [35] Astropy Collaboration *et al.* Astropy: A community Python package for astronomy. *Astronomy and Astrophysics* **558**, A33 (2013).
- [36] Astropy Collaboration *et al.* The Astropy Project: Building an Open-science Project and Status of the v2.0 Core Package. *The Astronomical Journal* **156**, 123 (2018).
- [37] Ginsburg, A. *et al.* Astroquery: An Astronomical Web-querying Package in Python. *The Astronomical Journal* **157**, 98 (2019).
- [38] Lightkurve Collaboration *et al.* Lightkurve: Kepler and TESS time series analysis in Python. *Astrophysics Source Code Library* ascl:1812.013 (2018).
- [39] Foreman-Mackey, D. Corner.py: Scatterplot matrices in Python. *The Journal of Open Source Software* **1** (2016).
- [40] Foreman-Mackey, D., Hogg, D. W., Lang, D. & Goodman, J. Emcee: The MCMC Hammer. *Publications of the Astronomical Society of the Pacific* **125**, 306–312 (2013). 1202.3665.
- [41] Carpenter, B. *et al.* Stan: A Probabilistic Programming Language. *Journal of Statistical Software* **76**, 1–32 (2017).
- [42] Van Hoey, S., van der Kwast, J., Nopens, I. & Seuntjens, P. Python package for model STructure ANalysis (pySTAN). *EGU General Assembly Conference Abstracts* **15**, EGU2013–10059 (2013).
- [43] Perez, F. & Granger, B. E. IPython: A System for Interactive Scientific Computing. *Computing in Science and Engineering* **9**, 21–29 (2007).
- [44] Kluyver, T. *et al.* Jupyter Notebooks – a publishing format for reproducible computational workflows. In Loizides, F. & Schmidt, B. (eds.) *Positioning and Power in Academic Publishing: Players, Agents and Agendas*, 87–90 (IOS Press, 2016).
- [45] van der Walt, S., Colbert, S. C. & Varoquaux, G. The NumPy Array: A Structure for Efficient Numerical Computation. *Computing in Science and Engineering* **13**, 22–30 (2011).
- [46] McKinney, W. Data Structures for Statistical Computing in Python. In *Proceedings of the 9th Python in Science Conference*, 51–56 (2010).

- [47] Hunter, J. D. Matplotlib: A 2D Graphics Environment. *Computing in Science and Engineering* **9**, 90–95 (2007).
- [48] Waskom, M. *et al.* Mwaskom/seaborn: V0.9.0 (July 2018). Zenodo (2018).
- [49] Seabold, S. & Perktold, J. Statsmodels: Econometric and Statistical Modeling with Python 5 (2010).
- [50] Salvatier, J., Wiecki, T. V. & Fonnesbeck, C. Probabilistic programming in Python using PyMC3. *PeerJ Computer Science* **2**, e55 (2016).
- [51] The Theano Development Team *et al.* Theano: A Python framework for fast computation of mathematical expressions. *arXiv:1605.02688 [cs]* (2016). 1605.02688.
- [52] Handberg, R. & Lund, M. N. Automated preparation of Kepler time series of planet hosts for asteroseismic analysis. *Monthly Notices of the Royal Astronomical Society* **445**, 2698–2709 (2014).
- [53] García, R. A. *et al.* Preparation of Kepler light curves for asteroseismic analyses. *Monthly Notices of the Royal Astronomical Society* **414**, L6–L10 (2011).
- [54] Christensen-Dalsgaard, J. ASTEC—the Aarhus STellar Evolution Code. *Astrophysics and Space Science* **316**, 13 (2008).
- [55] Huber, D. *et al.* Stellar Spin-Orbit Misalignment in a Multiplanet System. *Science* **342**, 331 (2013).
- [56] Buchhave, L. A. & Latham, D. W. The Metallicities of Stars with and without Transiting Planets. *The Astrophysical Journal* **808**, 187 (2015).
- [57] Chaplin, W. J. *et al.* Ensemble Asteroseismology of Solar-Type Stars with the NASA Kepler Mission. *Science* **332**, 213 (2011).
- [58] Harvey, J. High-Resolution Helioseismology. *Future Missions in Solar, Heliospheric & Space Plasma Physics* **235**, 199 (1985).
- [59] Chaplin, W. J. & Basu. *Asteroseismic Data Analysis: Foundations and Techniques* (Princeton University Press, Princeton, New Jersey, 2017), 1st edn.
- [60] Tassoul, M. Asymptotic approximations for stellar nonradial pulsations. *The Astrophysical Journal Supplement Series* **43**, 469 (1980).
- [61] Vrad, M., Mosser, B. & Samadi, R. Period spacings in red giants. II. Automated measurement. *Astronomy and Astrophysics* **588**, A87 (2016).
- [62] Hogg, D. W. Data analysis recipes: Probability calculus for inference. *arXiv e-prints* arXiv:1205.4446 (2012).
- [63] Hall, O. J. *et al.* Testing asteroseismology with Gaia DR2: Hierarchical models of the Red Clump. *Monthly Notices of the Royal Astronomical Society* **486**, 3569–3585 (2019). 1904.07919.

- [64] Mazumdar, A. *et al.* Measurement of acoustic glitches in solar-type stars from oscillation frequencies observed by Kepler. *The Astrophysical Journal* **782**, 18 (2014). 1312.4907.
- [65] Davies, G. R., Chaplin, W. J., Elsworth, Y. & Hale, S. J. BiSON data preparation: A correction for differential extinction and the weighted averaging of contemporaneous data. *Monthly Notices of the Royal Astronomical Society* **441**, 3009–3017 (2014).
- [66] Appourchaux, T. *et al.* Oscillation mode linewidths and heights of 23 main-sequence stars observed by *Kepler* (*Corrigendum*). *Astronomy & Astrophysics* **595**, C2 (2016).
- [67] Rasmussen, C. E. & Williams, C. K. I. *Gaussian Processes for Machine Learning*. Adaptive Computation and Machine Learning (MIT Press, Cambridge, Mass, 2006).
- [68] Toutain, T. & Appourchaux, T. Maximum likelihood estimators: An application to the estimation of the precision of helioseismic measurements. *Astronomy and Astrophysics* **289**, 649–658 (1994).
- [69] Gizon, L. & Solanki, S. K. Determining the Inclination of the Rotation Axis of a Sun-like Star. *The Astrophysical Journal* **589**, 1009 (2003).
- [70] Handberg, R. & Campante, T. L. Bayesian peak-bagging of solar-like oscillators using MCMC: A comprehensive guide. *Astronomy and Astrophysics* **527**, A56 (2011).
- [71] Anderson, E. R., Duvall, T. L. & Jefferies, S. M. Modeling of Solar Oscillation Power Spectra. *The Astrophysical Journal* **364**, 699 (1990).
- [72] Ballot, J., Garcia, R. A. & Lambert, P. Rotation speed and stellar axis inclination from p modes: How CoRoT would see other suns. *Monthly Notices of the Royal Astronomical Society* **369**, 1281–1286 (2006).
- [73] Ballot, J., Appourchaux, T., Toutain, T. & Guittet, M. On deriving p-mode parameters for inclined solar-like stars. *Astronomy & Astrophysics* **486**, 867–875 (2008). 0803.0885.
- [74] Kass, R. E. & Raftery, A. E. Bayes Factors. *Journal of the American Statistical Association* **90**, 773–795 (1995).
- [75] Girardi, L. *et al.* TRILEGAL, a TRIdimensional model of thE GALaxy: Status and Future. *Astrophysics and Space Science Proceedings* **26**, 165 (2012).
- [76] Girardi, L. *et al.* The Expected Stellar Populations in the Kepler and CoRoT Fields **39**, 125 (2015).
- [77] Mathur, S. *et al.* Revised Stellar Properties of Kepler Targets for the Q1-17 (DR25) Transit Detection Run. *The Astrophysical Journal Supplement Series* **229**, 30 (2017).
- [78] Berger, T. A. *et al.* The \$Gaia\$-\$Kepler\$ Stellar Properties Catalog I: Homogeneous Fundamental Properties for 186,000 \$Kepler\$ Stars. *arXiv:2001.07737 [astro-ph]* (2020). 2001.07737.

- [79] Gaia Collaboration *et al.* Gaia Data Release 2. Summary of the contents and survey properties. *ArXiv e-prints* arXiv:1804.09365 (2018).
- [80] Raghavan, D. *et al.* A Survey of Stellar Families: Multiplicity of Solar-type Stars. *The Astrophysical Journal Supplement Series* **190**, 1–42 (2010).
- [81] Betancourt, M. J. & Girolami, M. Hamiltonian Monte Carlo for Hierarchical Models. *arXiv:1312.0906 [stat]* (2013). 1312.0906.
- [82] Benomar, O. *et al.* Asteroseismic detection of latitudinal differential rotation in 13 Sun-like stars. *Science* **361**, 1231 (2018).
- [83] Beck, J. G. A comparison of differential rotation measurements - (Invited Review). *Solar Physics* **191**, 47–70 (2000).
- [84] Doyle, A. P., Davies, G. R., Smalley, B., Chaplin, W. J. & Elsworth, Y. Determining stellar macroturbulence using asteroseismic rotational velocities from Kepler. *Monthly Notices of the Royal Astronomical Society* **444**, 3592–3602 (2014).
- [85] Tayar, J. *et al.* Rapid Rotation of Low-mass Red Giants Using APOKASC: A Measure of Interaction Rates on the Post-main-sequence. *The Astrophysical Journal* **807**, 82 (2015).
- [86] Nielsen, M. B., Gizon, L., Schunker, H. & Karoff, C. Rotation periods of 12 000 main-sequence Kepler stars: Dependence on stellar spectral type and comparison with $v \sin i$ observations. *Astronomy and Astrophysics* **557**, L10 (2013).
- [87] Gizon, L. *et al.* Seismic constraints on rotation of Sun-like star and mass of exoplanet. *Proceedings of the National Academy of Science* **110**, 13267 (2013).
- [88] Chaplin, W. J. *et al.* Asteroseismic Determination of Obliquities of the Exoplanet Systems Kepler-50 and Kepler-65. *The Astrophysical Journal* **766**, 101 (2013).
- [89] Amard, L. & Matt, S. P. The Impact of Metallicity on the Evolution of Rotation and Magnetic Activity of Sun-Like Stars. *arXiv:2001.10404 [astro-ph]* (2020). 2001.10404.
- [90] Fleming, D. P., Barnes, R., Davenport, J. R. A. & Luger, R. Rotation Period Evolution in Low-mass Binary Stars: The Impact of Tidal Torques and Magnetic Braking. *The Astrophysical Journal* **881**, 88 (2019).
- [91] Maxted, P. F. L., Serenelli, A. M. & Southworth, J. Comparison of gyrochronological and isochronal age estimates for transiting exoplanet host stars. *Astronomy and Astrophysics* **577**, A90 (2015).
- [92] Gallet, F. & Delorme, P. Star-planet tidal interaction and the limits of gyrochronology. *arXiv e-prints* **1905**, arXiv:1905.06070 (2019).
- [93] Benbakoura, M., Réville, V., Brun, A. S., Le Poncin-Lafitte, C. & Mathis, S. Evolution of star-planet systems under magnetic braking and tidal interaction. *Astronomy and Astrophysics* **621**, A124 (2019).

- [94] Ceillier, T. *et al.* Rotation periods and seismic ages of KOIs - comparison with stars without detected planets from Kepler observations. *Monthly Notices of the Royal Astronomical Society* **456**, 119–125 (2016).
- [95] Metcalfe, T. S. & Egeland, R. Understanding the Limitations of Gyrochronology for Old Field Stars. *The Astrophysical Journal* **871**, 39 (2019). 1811.11905.
- [96] Lorenzo-Oliveira, D. *et al.* Constraining the evolution of stellar rotation using solar twins. *Monthly Notices of the Royal Astronomical Society* **485**, L68 (2019).

Author Contributions: O.J.H. led the project, with help from G.R.D., J.V.S., M.B.N. and W.J.C.. J.V.S. also led the development of the stellar population models. M.N.L., R.A.G. and S.K. both provided data or stellar models and along with J.T. assessed the validity of our asteroseismic results. L.A., A.B. and V.S. provided the assessment of the theoretical implications of the gyrochronology results. All authors have contributed to the interpretation of the data and the results, and all discussed and provided comments for all drafts of the paper.

Competing Interests: The authors declare that they have no competing financial interests.

Correspondence: Correspondence and requests for materials should be addressed to O.J.H.. (email: oliver.hall@esa.int).

Supplementary materials

Contents

1	Asteroseismic Methods	14
1.1	Asteroseismic Data	14
1.2	Asteroseismic Model	15
2	Gyrochronology Methods	23
2.1	Stellar Models	23
2.2	Bayesian Mixture Models	24
3	Results	27
4	Verifying asteroseismic results	27
4.1	Priors on rotational parameters	27
4.2	Comparisons to previous studies	28
4.3	Internal vs external rotation	31
5	Verifying consequences for gyrochronology	33
5.1	Rotational models for different stellar types	33
5.2	Limits of our stellar models	34
5.3	Systematic uncertainties from asteroseismology	35
5.4	Binaries and Planet Hosts	35
5.5	Evidence for Weakened Magnetic Braking in the literature	36

1 Asteroseismic Methods

1.1 Asteroseismic Data

For our asteroseismic power spectrum data we used the unweighted power spectra from the KASOC pipeline [52][§]. We did not apply any additional treatment to these data. For 16 Cyg A & B (KIC 12069424 and KIC 12069449) we used the KEPSEISMIC lightcurves [53][¶], which have significantly better signal-to-noise for these two stars.

For our sample, we used the asteroseismic ages obtained by **BASTA** [8, Bayesian STellar Algorithm] in the Kages and LEGACY catalogues. These ages have been obtained by comparisons of measured oscillation properties to stellar models, accounting for an expanded range of metallicities. **BASTA** is thoroughly compared to four other seismic modelling techniques in [24]. While uncertainties found through **BASTA** are typically higher than for other techniques, only **BASTA** and **ASTFIT** [54, Aarhus STellar Evolution Code] recover the radius, mass and age of the Sun, when applied to solar data. Although the uncertainties on **ASTFIT** ages are overall lower, they are not reported in [8] for the Kages sample. In order to maintain an

[§]Obtainable from the KASOC webpage.

[¶]Obtainable from MAST.

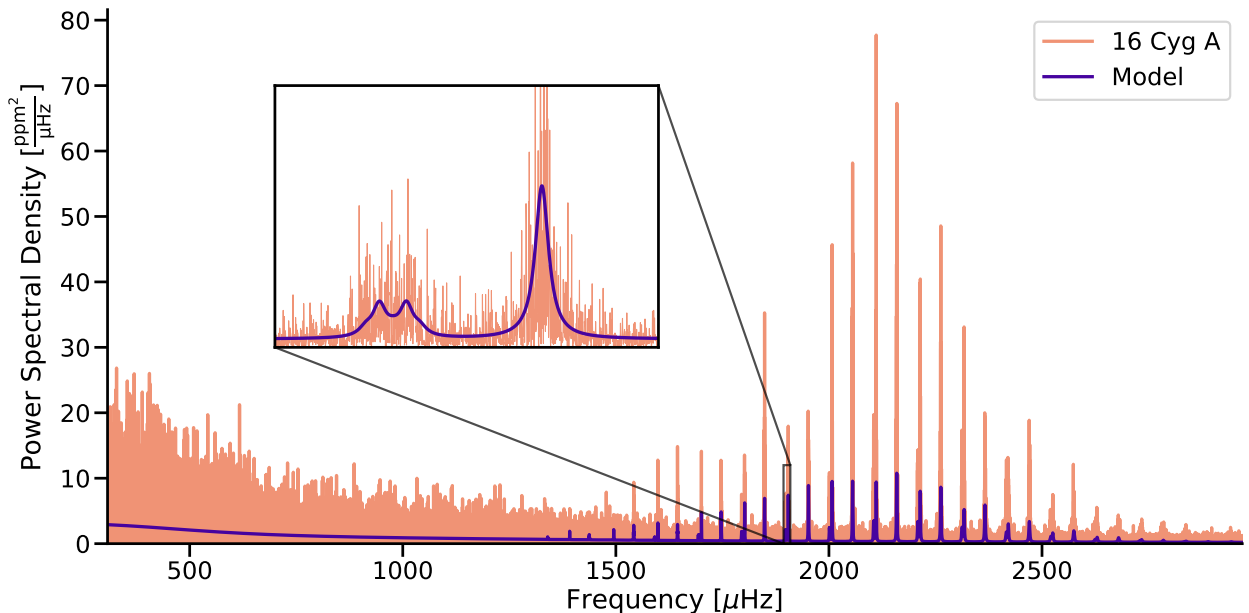


Figure 3: A power spectrum constructed from four years of *Kepler* observations of 16 Cyg A (KIC 12069424). Plotted over the top is the model resulting from the fit to the data described in this work. The model implements both the mode frequencies, seen on the right hand side of the plot, and the convective background, the effects of which are seen on the left. Low frequencies have been cropped out for clarity. *Inset*: A zoom in on a radial (right) and quadrupole (left) ($\ell = 0, 2$) pair of modes. The quadrupole mode is split into five components by the star’s rotation. Due to the star’s inclination angle with respect to us, two out of five peaks are more distinct. The height and spacing of the mode components is a function of the star’s rotational splitting ($0.56 \mu\text{Hz}$, equivalent to $P_{\text{rot}} = 20.5$ days) and angle of inclination (45°).

internally consistent stellar age sample, we used age results from **BASTA** for both the Kages and LEGACY samples.

For our stellar masses we used asteroseismic model masses obtained by **BASTA** reported in Kages and LEGACY, in order to maintain internal consistency with the age measurements. We note that age and mass posteriors from **BASTA** are correlated, but chose not to account for the unpublished correlations in this work. As described in the catalogue papers, for Kages stars atmospheric properties (T_{eff} and $[\text{Fe}/\text{H}]$) were measured through high-resolution spectroscopy reported in [55]. For LEGACY stars, atmospheric properties were similarly taken from [56] for most stars in the catalogue, and complemented by other values from the literature for the remaining stars [24, see Table 3].

1.2 Asteroseismic Model

In order to extract signatures of stellar rotation from the asteroseismic mode frequencies, we built a model that simultaneously treats the convective background ($B(\nu)$), the oscillations ($O(\nu)$), and the white noise (W) in the style of e.g. [11]. Our data, observed with *Kepler*, are also subject to the apodization (attenuation) of signals in the frequency-domain, where

we fit our model [57]. The apodization in power is given by

$$\eta^2(\nu) = \text{sinc}^2\left(\frac{\pi}{2} \frac{\nu}{\nu_{\text{nyq}}}\right), \quad (1)$$

where ν_{nyq} is the Nyquist frequency for the *Kepler* short cadence, which was treated as a free parameter in our model to account for gaps in the data. Apodization only affects signals with characteristic timescales, meaning that it does not affect the white noise level, only the oscillations and convective background components. Given the above, our comprehensive model for the power spectrum is

$$M(\nu) = W + \eta^2(\nu)[O(\nu) + B(\nu)]. \quad (2)$$

1.2.1 Convective Background

To model the convective background we used three Harvey components [58], which express the background in power as Lorentzian-like functions centered on zero frequency. The Harvey components take the form

$$H(\nu, a, b, x) = \frac{4a^2/b}{1 + (2\pi b\nu)^x}, \quad (3)$$

where a and b are the free parameters in our model, and x is fixed. The three Harvey components together form our background function as

$$B(\nu) = H(\nu, a, b, x = 4) + H(\nu, c, d, x = 4) + H(\nu, j, k, x = 2), \quad (4)$$

where we have labeled parameters for the separate components. The $x = 2$ term here contributes to the background at high frequencies, whereas the $x = 4$ terms contribute the background at low frequencies.

1.2.2 Modes of Oscillation

Modes of oscillation appear in the power spectrum as Lorentzian peaks [59]. Due to stellar rotation, each mode with an angular degree of $\ell > 0$ is split into its $(2\ell + 1)$ Lorentzian components, labeled by m , the azimuthal order. For all $\ell = (0, 1, 2)$ modes identified in [22, 23] we add a (set of) Lorentzian(s) to our model, building a composite model representing all visible modes. The construction of our oscillation model takes the form

$$O(\nu) = \sum_n \sum_{\ell} \sum_{m=-\ell}^{\ell} \frac{H_{n,\ell,m}}{1 + \frac{4}{\Gamma_{n,\ell}^2}(\nu - \nu_{n,\ell,m})^2}, \quad (5)$$

where n is the radial order of a mode (i.e. the overtone number of the oscillation), $H_{n,\ell,m}$ is the height of the mode, $\Gamma_{n,\ell}$ is the linewidth of the mode (approximated to be equal for all split components at a single n and ℓ) and $\nu_{n,\ell,m}$ is the frequency of the mode. The range of n differs per star depending on how many radial orders were reported in LEGACY or Kages, and the range of ℓ depends on how many angular degrees were reported for the corresponding radial order.

1.2.3 Mode Frequencies and Rotational Splitting

The mode frequencies of main sequence stars are described by the asymptotic expression [60, 61]. The asymptotic expression defines the locations of the modes as regularly spaced, with structured deviation around ν_{\max} , the frequency of maximum oscillation amplitude. The expression takes the form

$$\nu_{n,\ell,m} = \Delta\nu \left(n + \epsilon + \delta\nu_{0,\ell} + \frac{\alpha}{2} \left(n - \frac{\nu_{\max}}{\Delta\nu} + \epsilon \right)^2 \right) + m\nu_s, \quad (6)$$

where $\Delta\nu$ is the large frequency separation between two consecutive radial orders, ϵ is a phase offset, $\delta\nu_{0,\ell}$ is the small frequency separation between two oscillation modes of different ℓ at the same radial order, α describes the curvature of the spacing around ν_{\max} , and ν_s is the rotational splitting. Note that here we have expressed the small separation $\delta\nu_{0,\ell}$ as a fraction of $\Delta\nu$. In order to improve the computational efficiency of this analysis, we fixed $\Delta\nu$ to the values reported in LEGACY and Kages.

Instead of calculating mode frequencies directly from Equation 6 for the model, we treated the individual mode frequencies as parameters as well, drawn from Equation 6. This is called a ‘latent parameter’ implementation [62, 63], as it forms a step between the parameters we want to draw inference on (also called hyperparameters) and our data. The parameters $\nu_{n,\ell,m}$ were allowed to vary within an uncertainty σ_ℓ , which has a single value for each angular degree and also varied as a free parameter. This allowed us to account for small shifts in frequency due to sudden changes in the stellar structure [64, called acoustic glitches]. The mode frequency latent parameters were drawn from a normal distribution using Equation 6 as its mean function, as

$$\nu_{n,\ell,m} \sim \mathcal{N}(\nu_{n,\ell,m}, \sigma_\ell), \quad (7)$$

where the expression $\nu_{n,\ell,m}$ on the right hand side represents the contents of Equation 6, and \mathcal{N} represents a normal distribution with a mean equal to $\nu_{n,\ell,m}$ and a standard deviation equal to σ_ℓ . The symbol ‘ \sim ’ indicates that the parameters on the left hand side of the equation are drawn from the probability distribution on the right hand side. This notation will be used throughout this paper.

1.2.4 Mode Linewidth

The linewidths of asteroseismic p modes vary roughly as a function of mode frequency, and do so slowly relative to $\Delta\nu$. This can be expressed as an empirical relation [65, 66, 23]. However, this relation has six free parameters, none of which are directly relevant to this work. Instead of fitting this relation, we chose to employ a more flexible Gaussian Process [67, GP] to act as a prior on the linewidths. This can be considered as us modelling the linewidths as correlated measurements. As our GP covariance kernel we used a Squared Exponential Kernel to capture the slight periodicity of linewidth with frequency, as

$$K_{i,j} = \rho^2 \exp \left[-\frac{(n_{f,i} - n_{f,j})^2}{2L^2} \right], \quad (8)$$

where n_f is the fractional radial order of a given mode. For each star, the overtone numbers n were rescaled to be between 0 (for the lowest n) and 1 (for the highest n)[‡]. This approximation was used to describe the change in linewidth as a function of frequency without depending on the exact frequencies of the modes. $K_{i,j}$ represents an element of the covariance matrix \underline{K} , describing the covariance between two values of linewidth at different fractional radial orders. The GP kernel has two hyperparameters: ρ , which determines the spread of the kernel, and L , which determines the length scale in terms of n_f . The length scale was significantly larger than the large frequency separation ($\Delta\nu$) in all cases, and so we considered the use of fractional radial orders a valid approximation in this model.

A linear function was used for the mean of the GP, as

$$\mu = m \times n_f + c, \quad (9)$$

where m and c are the slope and intercept of the line. The linewidth latent parameters were then drawn from the multivariate probability distribution

$$\Gamma \sim \mathcal{N}(\mu, \underline{K}), \quad (10)$$

where Γ represents the linewidths of all the modes in the model. The parameters m , c and ρ were marginalised over, whereas L was fixed to a pre-determined value.

1.2.5 Mode Heights and Angle of Inclination

The height in power of each mode, $H_{n,\ell,m}$, varies not only as a function of distance in frequency from ν_{\max} , but also due to observation conditions, such as inclination angle and passband. In our model, we treated $H_{n,\ell,m}$ as a deterministic parameter, as

$$H_{n,\ell,m} = \varepsilon_{\ell,m}(i) \frac{2(A_{n,\ell})^2}{\pi\Gamma_{n,\ell}}, \quad (11)$$

where $\varepsilon_{\ell,m}(i)$ modulates the height as a function of inclination angle (i) (see below), and $A_{n,\ell}$ and $\Gamma_{n,\ell}$ are the mode amplitude and linewidth respectively for a given radial order and angular degree. Instead of modeling and modulating height directly, we instead sampled in amplitude and linewidth. This approach mitigates the correlations between height and linewidth in the sampling process [68].

As done above for the mode frequencies and linewidths, the mode amplitudes $A_{n,\ell}$ were also treated as latent parameters drawn from a probability distribution governed by hyperparameters. We used a Gaussian function $G(\nu)$, centered on ν_{\max} , so that

$$G(\nu) = A \times \exp \left[-\frac{(\nu - \nu_{\max})^2}{2w^2} \right], \quad (12)$$

where A is the amplitude at ν_{\max} , and w is the width of the Gaussian, both free parameters in our model. The mode amplitude latent parameters were then drawn from the probability distribution

$$A_{n,\ell} \sim \mathcal{N}(G(\nu_{n,\ell}) \times V_\ell, \sigma_A), \quad (13)$$

[‡]Overtone of $\ell = 2$ modes were increased by 1 to ensure this approximation applied to all modes.

where V_ℓ is a free parameter for the mode visibility of different angular degrees, which should be consistent for all *Kepler* observations. The mode visibility for V_0 is fixed at 1, and $V_{1,2}$ are treated as free parameters. The parameter σ_A , the uncertainty on the distribution, is also a free parameter, and takes the same value for all amplitudes regardless of angular degree.

The angle of inclination of a star with respect to Earth changes the net perturbation by a given mode when integrated across the stellar disc, changing the amplitudes of modes of different azimuthal orders. This is a geometric problem, and is expressed by $\varepsilon_{\ell,m}(i)$, which takes the form [69]

$$\varepsilon_{\ell,m}(i) = \frac{(\ell - |m|)!}{(\ell + |m|)!} \left[P_\ell^{|m|}(\cos(i)) \right]^2, \quad (14)$$

where $P_\ell^{|m|}$ are associated Legendre functions. For the first three angular degrees, Equation 14 takes the form [70]

$$\begin{aligned} \varepsilon_{0,0}(i) &= 1, \\ \varepsilon_{1,0}(i) &= \cos^2(i), \\ \varepsilon_{1,\pm 1}(i) &= \frac{1}{2} \sin^2(i), \\ \varepsilon_{2,0}(i) &= \frac{1}{4} (3 \cos^2(i) - 1)^2, \\ \varepsilon_{2,\pm 1}(i) &= \frac{3}{8} \sin^2(2i), \\ \varepsilon_{2,\pm 2}(i) &= \frac{3}{8} \sin^4(i), \end{aligned} \quad (15)$$

where the sum of available components for a single ℓ are normalized to one.

1.2.6 Likelihood Function

If data have Gaussian noise in the time domain, they will appear in the frequency domain with noise following a χ^2 distribution with two degrees of freedom [?, χ_2^2 hereafter] woodard1984. The noise properties of χ_2^2 distributed data are multiplicative, and require a specific treatment when fitting a model. As our frequency bins can be approximated to be independent, we used the likelihood function [71],

$$\ln p(\mathcal{P}|M) = \sum_{j=0}^{N-1} \left[\ln[M_j(\nu)] + \frac{\mathcal{P}_j}{M_j(\nu)} \right], \quad (16)$$

where \mathcal{P} is the power spectral density (and thus our data), and $M(\nu)$ represents our model. The subscript j denotes an individual datum, for a total of N data. We have omitted the dependence of the model $M(\nu)$ on its parameters, for clarity. This equation is functionally equivalent to the evaluation of a gamma distribution of the form $\gamma(\mathcal{P}|1, \beta)$, where $\beta = 1/M(\nu)$, which is the implementation we used in the sampling process.

1.2.7 Fitting the convective background

Fitting the convective background, apodization and white noise component must be done for the full range of the power spectrum in order to be accurately constrained. However, fitting a single model to the full range of frequencies is computationally inefficient when we are interested in the modes of oscillation, as these occupy a relatively small range of frequencies.

In order to speed up this process, the background was first fit independently to a subset of our data for each star. This subset was created by removing all frequencies within a range $0.1 \times \Delta\nu$ below and above the minimum and maximum mode frequencies reported in LEGACY and Kages. For KIC 3427720 we also removed frequencies in the range $90 \mu\text{Hz} < \nu < 400 \mu\text{Hz}$, where there were large peaks not of asteroseismic origin, skewing the background fit.

For each star the model function (see Eq. 2) was fit, as

$$M_B(\nu) = W + \eta^2(\nu)B(\nu), \quad (17)$$

where $B(\nu)$ is the background model described in Equation 4. The parameter components of our background fit are then $\phi_B = \{\log(a), \log(b), \log(c), \log(d), \log(j), \log(k), W, \nu_{\text{nyq}}\}$, where the parameters of the Harvey components were sampled in log space. The model was fit to the background data using PyStan [42], run for 10,000 iterations on each star**.

1.2.8 Obtaining First Guesses and Prior Values

In order to utilise some of the prior measurements of our targets without using them as hard constraints on our parameters, some of our model equations were fit to LEGACY and Kages data to obtain first guesses and mean values on hyperparameter priors.

For first guesses for parameters in the asymptotic expression, we fit Equation 6, *not* including the rotational component $m\nu_s$, to the $\ell = (0, 1, 2)$ mode frequencies reported in LEGACY and Kages for each star, using their reported uncertainties. This yielded estimates of $\hat{\epsilon}$, $\widehat{\delta\nu_{01}}$, $\widehat{\delta\nu_{02}}$ and $\hat{\alpha}$, where the hat symbol ‘ $\hat{}$ ’ indicates a prior value (e.g. $\hat{\nu}_{\text{max}}$ is taken from LEGACY or Kages). While not precise, as we did not mitigate any perturbations due to acoustic glitches (sudden changes in interior sound speed, which the latent parameter treatment takes care of in the full model), these rough results act as functional first guesses and prior mean values. The relation was fit to each star using PyMC3 [50] using 5000 iterations on 4 chains.

To obtain first guesses for the parameters used to set the GP prior on linewidth, we fit a GP constructed as in Equation 10 to the linewidths of the $\ell = 0$ modes reported in LEGACY. Linewidths were not reported for the other angular degrees in LEGACY, but the estimates may be generalised to other ℓ , as linewidth is a strong function of frequency. The relation was fit to each star using PyMC3 using 2500 iterations on 4 chains.

Fitting the LEGACY linewidths yielded rough estimates of \hat{m} , \hat{c} , $\hat{\rho}$ and L for each star. As is noted in Equation 10, L was fixed to this fit value when fitting our full model to our data. For stars in Kages, for which no linewidths were reported, we instead fixed these prior values to $\hat{m} = 1$, $\hat{c} = 0.5$, $\hat{\rho} = 0.1$, and the length scale to $L = 0.3$. These values were chosen to reflect those found for the LEGACY stars.

**These PyStan runs were initiated with a random seed of 11, as were all other random processes in this work.

Finally, we obtained prior values for the Gaussian function describing the distribution of mode amplitudes around ν_{\max} . The mode amplitude of the highest peak in the spectrum was used for the amplitude, which was typically at or near ν_{\max} . For the width of the Gaussian we used the empirical function [23]

$$\hat{w} = 0.25 \times \nu_{\max} . \quad (18)$$

For the mode visibilities, we used $\hat{V}_1 = 1.2$ and $\hat{V}_2 = 0.7$, which reflect the results for these parameters reported in the LEGACY catalogue.

1.2.9 Priors on our Hyperparameters

Given our first guesses and measured prior values, we can define the prior probabilities of the hyperparameters on which our model depends. For the mode frequency hyperparameters, these are

$$\begin{aligned} \nu_{\max} &\sim \mathcal{N}(\hat{\nu}_{\max}, 10) , \\ \epsilon &\sim \mathcal{N}(\hat{\epsilon}, 1) , \\ \alpha &\sim \ln \mathcal{N}(\ln(\hat{\alpha}), 0.01) , \\ \delta\nu_{01} &\sim \ln \mathcal{N}(\ln(\widehat{\delta\nu_{01}}), 0.1) , \\ \delta\nu_{02} &\sim \ln \mathcal{N}(\ln(\widehat{\delta\nu_{02}}), 0.1) , \\ \sigma_{0,1,2} &\sim \mathcal{C}_{1/2}(\beta = 2) , \end{aligned} \quad (19)$$

where $\ln \mathcal{N}$ represents a log-Normal distribution and $\mathcal{C}_{1/2}$ represents a half-Cauchy distribution, and other symbols are as described above. All three hyperparameters $\sigma_{0,1,2}$ describing the uncertainty on the latent parameters of different angular degree were subject to the same prior.

For the mode linewidths, our hyperparameter priors took the form

$$\begin{aligned} m &\sim \mathcal{N}(\hat{m}, 1) , \\ c &\sim \mathcal{N}(\hat{c}, 1) , \\ \rho &\sim \ln \mathcal{N}(\ln(\hat{\rho}), 0.1) , \end{aligned} \quad (20)$$

where the conventions are the same as above. For our mode amplitudes, they took the form

$$\begin{aligned} w &\sim \ln \mathcal{N}(\ln(\hat{w}), 10) , \\ A &\sim \ln \mathcal{N}(\ln(\hat{A}), 1) , \\ V_1 &\sim \ln \mathcal{N}(\ln(\hat{V}_1), 0.1) , \\ V_2 &\sim \ln \mathcal{N}(\ln(\hat{V}_2), 0.1) , \\ \sigma_A &\sim \mathcal{C}_{1/2}(\beta = 1) . \end{aligned} \quad (21)$$

As the convective background had already been fit to our data excluding the region where the modes are present, the results from that fit could be used as extremely informative priors

on our fit to the region containing the modes, where there is little information present to constrain the background. To do so, we modeled the background parameters ϕ_B in our full model as being drawn from a multivariate normal distribution as

$$\phi_B \sim \mathcal{N}(\hat{\phi}_B, \underline{\Sigma}_{\hat{\phi}_B}), \quad (22)$$

where $\hat{\phi}_B$ are the median values of our posterior distributions from our prior background fit, and $\underline{\Sigma}_{\hat{\phi}_B}$ is the full covariance matrix of all the posterior distributions from our prior background fit, taking into account the correlations between the different Harvey components.

Finally, we defined the priors on the rotational parameters: the mode splitting (ν_s), and the inclination angle (i). In order to give these an appropriate treatment, we made two reparameterizations. First, we sampled the projected rotational splitting, $\nu_s \sin(i)$, which is more efficiently sampled due to the strong correlations between i and ν_s [72, 73]. A prior was applied over this as

$$\nu_s \sin(i) \sim \ln \mathcal{N}(\ln(0.75), 0.75), \quad (23)$$

where conventions are as above. This subjective prior was chosen to reflect that most stars will have a solar-like rotation, with a long tail to allow for the fastest rotators. Second, we sampled in $\cos(i)$, and gave this a prior of

$$\cos(i) \sim \mathcal{U}(0, 1), \quad (24)$$

which is equivalent to stating that probability to observe an inclination angle i is equal to $\sin(i)$. Here, the $\mathcal{U}(0, 1)$ indicates a uniform prior between 0 and 1. Using a uniform prior on $\cos(i)$ allowed us to account for the geometric effect that stars with a large inclination angle with respect to us are more common [59].

1.2.10 Fitting procedure

Using our prior information and model described above, we fit Equation 2 to our data \mathcal{P} , using the likelihood function described in Section 1.2.6.

In order to speed up the fitting process, we only applied our model to the region of the power spectrum that contains visible modes of oscillation. We created this subset by removing all frequencies outside a range $0.25 \times \Delta\nu$ below and above the minimum and maximum mode frequencies reported in LEGACY and Kages. This region overlaps minimally with the data used to fit for our prior information of the convective background (see Section 1.2.7), so that both model fits are independent.

To improve computational efficiency, we reduced the number of oscillation modes being fit in five targets. For 16 Cyg A & B, KIC 7970740 and KIC 8478994, we excluded any modes with a Bayes Factor ($\ln(K)$) of less than 6, as reported in LEGACY [74, 22, 23]. For KIC 8478994, which is reported without a value for $\ln(K)$ in Kages, we only included modes of an overtone number that contained a detection for all of $\ell = (0, 1, 2)$, retaining 5 sets of higher signal-to-noise overtones. We do not expect this reduced scope to bias our results, although they may reduce the precision on our measured rotation rates.

We fit our model to our power spectrum data with PyMC3, using 2500 iterations each on 4 chains. An example of our model fit to an asteroseismic power spectrum of 16 Cyg A is shown in Figure 3.

2 Gyrochronology Methods

2.1 Stellar Models

The braking models used in this work have several parameters that inform the rotational evolution. These are: a normalization factor to reproduce the solar rotation (f_k); a disk locking timescale (T_{disk}) and period (P_{disk}) which together regulate the stellar angular velocity during the pre-main sequence; the critical angular velocity that marks the transition from saturated (rapidly rotating) to unsaturated (slowly rotating) regimes (ω_{crit}), and the critical Rossby number, above which stars conserve angular momentum (Ro_{crit}), mentioned above. T_{disk} , P_{disk} and ω_{crit} are calibrated to match the behavior in young open clusters, but have little impact on the rotational evolution beyond ≈ 1 Gyr in solar-mass stars. Both f_k and Ro_{crit} affect the late-time evolution. Both models adopt $\omega_{\text{crit}} = 3.4 \times 10^{-5} \text{ s}^{-1}$, $P_{\text{disk}} = 8.1$, $T_{\text{disk}} = 0.28$ and $f_k = 6.6$. In the weakened magnetic braking model, $Ro_{\text{crit}} = 1.97$. For further details, see [1] and [2, 18].

Instead of comparing asteroseismic measurements of age and rotation directly to rotational models of individual stars, we instead compared them to synthetic populations based on rotational models, similar to those presented in [18], with some adaptations. To construct a synthetic population of rotating stars, [18] applied the rotational braking laws described above to a galactic population model. Their approach used a TRILEGAL [75] Milky-Way simulation of the *Kepler* field, using the standard population values intended for this purpose from [76]. Stars from the TRILEGAL simulations were then drawn randomly in bins until they matched observations of stellar parameters of the *Kepler* field [77]. This aimed to replicate the *Kepler* selection effect, by ensuring the TRILEGAL population properties matched those observed in the *Kepler* field.

We used the same approach here, with two changes. First, we updated the distribution of stellar parameters matched to the TRILEGAL populations. Instead of [77], we used the [78] temperatures and luminosities, and 2MASS *K*-band magnitudes as our stellar parameter distributions for the *Kepler* field, which are more accurate following the use of *Gaia* DR2 parallaxes [79]. The TRILEGAL simulation was matched to the [78] sample using a nearest-neighbours approach (as opposed to binning), based on the density of stars on the HR diagram.

Second, we made further changes to account for possible binarity in the the [78] sample. If the first step is performed blindly, blended binaries in the sample cause an overestimation of the number of old stars. In order to overcome this, we:

1. blended the TRILEGAL stars with binary companions drawn from a flat mass-ratio distribution, using the binary fraction of [80],
2. recalculated the ‘observed’ luminosities and magnitudes assuming that each binary pair was blended, and
3. shifted these stars’ temperatures following the *g-K* relation presented in [78].

This new distribution was used for the nearest-neighbour matching. Once drawn we dropped the binary companion and used the true TRILEGAL properties of those stars. For stars where the mass of the companion was $M < 0.4 M_{\odot}$, binary contributions were ignored. Every binary was assumed to result in a blend, regardless of separation. This results in slightly more young stars than reality, because young, blended binary systems contaminate regions of the HR diagram where one expects to find old stars, and the number of blends is overestimated by assuming every binary system is a blend.

Our asteroseismic sample of stars with short cadence observations are subject to additional selection functions not included in the creation of the model populations above. We did *not* explicitly account for these asteroseismic selection functions in our model, by design. Both the standard and WMB models contain stars with the same fundamental parameters (mass, radius, effective temperature, metallicity) but a different period based on the choice of rotational evolution prescription. Applying an asteroseismic selection function that depends on these fundamental parameters [57] would apply an identical prior to both models, therefore providing no net effect on our posterior distribution. Additionally, we expected any seismic selection function to be relatively flat (and therefore uninformative) on a star-by-star scale, on which we run our model analysis (as opposed to a population scale, see below).

2.2 Bayesian Mixture Models

In order to determine whether weakened magnetic braking occurs on the main sequence, we compared our sample of seismic age and rotation, along with temperature, metallicity and mass, to the two stellar population models of the *Kepler* field adapted from [18], discussed above. Both stellar models were evaluated in a Bayesian framework, with the rationale of determining which of the two models (standard or WMB) is most likely to reproduce our observed data. Each model sample contained temperature (T_{eff}), mass (M), age (t), metallicity ($[\text{Fe}/\text{H}]$) and rotation (P) information.

In order to draw probabilistic inference about the models, we built a five-dimensional Kernel Density Estimate (KDE) of both model populations using the `statsmodels` package [49]. We used a band-width (setting the resolution of the KDE) of $0.02 M_{\odot}$ in mass, 10 K in T_{eff} , 0.01 dex in $\ln(t)$, 0.01 dex in $[\text{Fe}/\text{H}]$ and 0.01 dex in $\ln(P)$. Note that age and rotation were treated in log space, where the posterior estimates from asteroseismology more closely resemble normal distributions. This approach translates the population models to a probability distribution we can use in a Bayesian framework.

We evaluated our data against both models simultaneously by treating the data as being drawn from a mixture of both model KDEs. In this mixture model structure, the two KDEs were modulated by a weighting factor, P_s . In the limit $P_s \rightarrow 1$, the data are most likely drawn from the standard model. In the limit $P_s \rightarrow 0$, the data are most likely drawn from the WMB model.

The posterior probability of obtaining P_s and additional parameters θ given our data \mathcal{D} is $p(P_s, \theta | \mathcal{D})$. Using Bayes equation, we can express this as:

$$p(P_s, \theta | \mathcal{D}) \propto p(\mathcal{D} | \theta) p(\theta | P_s, \kappa_s, \kappa_{\text{WMB}}) p(P_s), \quad (25)$$

where κ_s and κ_{WMB} are the KDE functions for the standard and WMB models respectively, and θ here are parameters, $\theta = \{M, T_{\text{eff}}, \ln(t), [\text{Fe}/\text{H}], \ln(P)\}$. As done above for the astero-

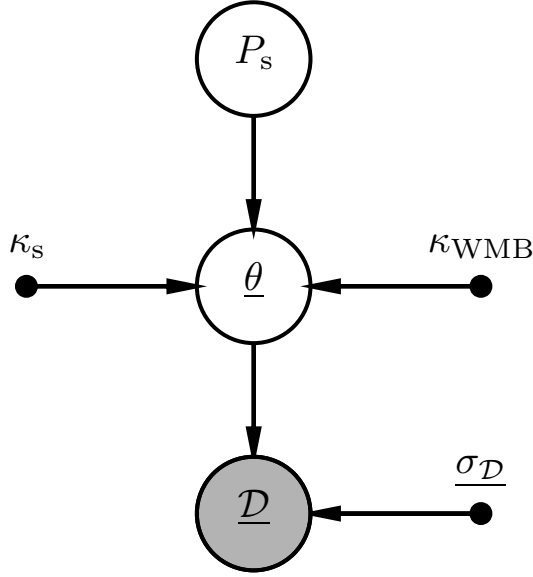


Figure 4: A probabilistic graphical model (PGM) represented algebraically in Equation 25. The shaded circle indicates observed data, and solid black points represent other fixed information, such as the KDEs and observational uncertainties. The remaining circles represent parameters. The underline indicates that the symbol represents a set of parameters or data. Here, κ_s and κ_{WMB} represent the KDEs of standard and WMB model populations respectively. P_s is the mixture model weighting factor. The latent parameters $\underline{\theta}$, our observations $\underline{\mathcal{D}}$ and their uncertainties $\underline{\sigma_{\mathcal{D}}}$ include temperature (T_{eff}), mass (M), log-age ($\ln(t)$), metallicity ($[\text{Fe}/\text{H}]$) and log-rotation ($\ln(P)$). This model is *hierarchical*, as all the latent parameters are drawn from the common probability distribution set by P_s and described in Equation 26.

seismic model, the parameters θ may be referred to as latent parameters, as they form a step between the parameter we want to infer (P_s) and our data. Using this approach allowed our model to properly take into account the observational uncertainties on the data.

The second component on the right hand side of Equation 25 describes the probability of obtaining our latent parameters θ given our KDEs and the mixture model weighting parameter P_s , and is described by the mixture model

$$p(\theta|P_s, \kappa_s, \kappa_{\text{WMB}}) = P_s \times \kappa_s(\theta) + (1 - P_s) \times \kappa_{\text{WMB}}(\theta), \quad (26)$$

where all parameters are as described above. This probability function describes a distribution that is a mixture of both KDEs. While the KDEs are constant, P_s is a free parameter, and so the shape of this distribution can vary. The latent parameters θ are drawn from this distribution, and therefore from some combination of the two stellar models.

The first component in Equation 25 describes the likelihood of obtaining the parameters θ given our data and their observational uncertainty. It takes the form

$$p(\mathcal{D}|\theta) = \mathcal{N}(\mathcal{D}|\theta, \sigma_{\mathcal{D}}), \quad (27)$$

a normal distribution evaluating the latent parameters θ against the observations, with observational uncertainty $\sigma_{\mathcal{D}}$. This approach means that in each parameter space (such as age), the age drawn from the stellar model mixture is entered into the likelihood equation with our static observations. The value of this equation (and thus the likelihood) will increase if θ is closer to the observations, and the mixture model will be modulated in a manner that maximises this probability, inferring whether one stellar model is more likely to produce our data than the other.

The final term, $p(P_s)$, represents the prior on the mixture model weight, which is uniform between 0 and 1. A visual representation of our model is shown in Figure 4.

Typically, this model would evaluate all stars in our sample against the stellar models simultaneously for a single posterior estimate of P_s . At 95 stars, in 5 parameter spaces, this totals 476 free parameters to marginalise over. This is not an issue for Hamiltonian Monte Carlo [81, HMC], however the use of KDE functions, over which a probabilistic gradient can not be measured, reduces HMCs effectiveness. Alternative Markov Chain Monte Carlo techniques [40, MCMC] can more efficiently sample the KDE functions, but can not treat the large number of hierarchical parameters. To overcome this, we fit our model to each star to obtain an independent individual posterior distribution for P_s , and multiplied these post hoc to obtain a combined posterior. This comes with the benefit of easily allowing us to calculate the combined posterior for different stellar classifications (see Section ??), at the expense of the ability to marginalise for a single value of P_s directly.

2.2.1 Fitting procedure

The parameter space of the stellar models was reduced before calculating the KDEs. These cuts were made in M , T_{eff} , $\ln(t)$ and $[\text{Fe}/\text{H}]$, removing any stars in the models that fell more than $3 \times \sigma_{\mathcal{D}}$ outside the observations. Our observables M , t and P have asymmetric uncertainties from the Bayesian asteroseismic analysis. We used the larger of the reported uncertainties on each parameter as $\sigma_{\mathcal{D}}$ in each parameter space.

KIC 6278762 was excluded from this stellar model analysis, because its age fell more than 3σ outside of the highest age in the stellar models^{††}, and KICs 7106245 and 8760414 were excluded for the same reason due to low metallicities outside the functional range of the stellar models (-0.99 and -0.92 respectively).

We fit our model Equation 25 using `emcee` [40], using 32 walkers for a total of 7500 samples per walker, of which the first 2500 were discarded as a burn-in.

After fitting, we took a normalised histogram of the posterior estimate of P_s for each star, using 100 bins. In this histogram, each bin approximated the value of the posterior function for P_s . The array of 100 bins for all stars were multiplied, resulting in an approximation of the joint posterior probability function for P_s given all stars in the ensemble.

3 Results

bla bla short shpiel about which values were included and which weren't

4 Verifying asteroseismic results

4.1 Priors on rotational parameters

In our Bayesian analysis, we have placed weakly informative priors on our sampled rotational parameters, $\nu_s \sin(i)$ and $\cos(i)$ (see Section 1.2). The prior is especially important for the angle of inclination, which is hardest to infer from the data. We are able to validate the robustness of our asteroseismic results by confirming that their posterior distributions are data-dominated, and not prior-dominated. We can do so by comparing the 68% credible regions of the posterior estimates of $\nu_s \sin(i)$ and i against the 68% credible regions of their priors.

A comparison between prior and posterior is shown for 94 stars in $\nu_s \sin(i)$, i and P_{rot} in Figure ??, arranged by age. In the Figure, results with means and error bars that closely resemble the prior distribution can be interpreted as prior-dominated (i.e. poorly informed by the data). The projected splitting, $\nu_s \sin(i)$, is overall well constrained, with only one star appearing prior dominated. This is expected, as the projected splitting is what we observe on the star before decoupling inclination and rotation. The angle of inclination i , sampled as $\cos(i)$, more closely follows the prior distribution in most cases. Combining the two, the rotation period P_{rot} has no stars directly corresponding to the effective prior on period, and globally follows a trend with increasing age. The three outliers with fast rotation at late ages (KICs 6603624, 8760414 and 8938364) are discussed in more detail in Section 4.2.

The rotation rates as presented in this work are a product of our Bayesian sampling of both projected splitting and angle of inclination. As seen in Figure ?? there are instances where i or $\nu_s \sin(i)$ closely resemble the prior (and are therefore prior-dominated). There are no cases of this when looking at the resulting period measurements, as they will have been informed by at least one strongly data-driven parameter (judging from Figure ??, commonly $\nu_s \sin(i)$).

^{††}This is a metallicity issue, as the oldest stars have metallicities outside the range of the rotational model grids.

From this, we conclude that our ensemble of asteroseismic rotation is not strongly dominated by the priors imposed on projected splitting and inclination in our Bayesian analysis.

4.2 Comparisons to previous studies

In order to validate our results, we compared our rotational parameters to those obtained in the literature, as well as those resulting from the work presented in LEGACY and Kages, which were unreported and received through private communication by the authors of the catalogue papers.

Comparisons with LEGACY and Kages are shown in Figure 5 for projected splitting, inclination angle, and rotation period. In all three cases we show the fractional difference between the values obtained in this work and those from LEGACY and Kages. On the right of Figure 5, we show the distribution of the fractional differences for the three parameters. The projected splitting is in good agreement with both studies, however LEGACY finds slightly lower $\nu_s \sin(i)$ for the faster rotators, deviating from our work by over 1σ . Neither LEGACY nor Kages used a spatially isotropic prior for the inclination angle in their analyses, instead opting for a uniform prior. As posterior estimates of inclination angle are only loosely data-driven, the introduction of an isotropic prior should result in our analysis reporting globally higher inclination angles. This effect is seen in the comparisons of both inclination angles and rotation rates for the LEGACY stars, where we find overall lower rotation rates compared to LEGACY for stars at very similar $\nu_s \sin(i)$.

A number of stars are excluded from Figure 5 and compared individually as extreme outliers: KICs 5094751, 6196457, 8349582, 8494142, 8554498, 105114430 and 11133306 all have fast rotation rates (< 5 days) in Kages, but are found to have a broader spread of rotation rates in this work. At similar values for $\nu_s \sin(i)$, Kages found much lower inclination angles with highly asymmetrical uncertainties. Based on a comparison between the summary statistics of these stars, we conclude that the results found in this work have better marginalised over inclination angle, improving our measure of rotation.

Conversely, KICs 6603624, 8760414 and 8938364 have extremely slow rotation periods in LEGACY, but extremely *fast* (< 3 days) in this work. KICs 8760414 and 8938364 are excluded from the gyrochronology analysis below based on checks for \hat{R} and the number of effective samples. Both stars have ages greater than 10 Gyr, making their fast rotation rates highly unlikely under any model of rotational evolution. The posterior estimate of P for KIC 6603624 is well-defined in our analysis, but with an age of 7.8 Gyr, its measured rotation of 1.2 days is also highly unlikely under any model of rotational evolution. The LEGACY estimate of rotation is similarly extreme at 378 days. These three stars have the lowest inclination angles in our sample ($< 10^\circ$), at which point the power in the split components of the seismic modes is so low that it becomes difficult to probe the measure of splitting^{‡‡}. In cases such as these with lower signal-to-noise, spurious peaks may be interpreted as split components.

We also compared our asteroseismic estimates of stellar rotation with similar studies in the literature, shown in Figure 6. These included: [11], a study of the binary solar analogues 16 Cyg A & B; [10], which our catalogue shares 5 stars with; and [82], an asteroseismic study

^{‡‡}The split components for these stars will have a height roughly 3% of the central mode. For comparison, for the next lowest inclined star at 17° , this rises to 10%.

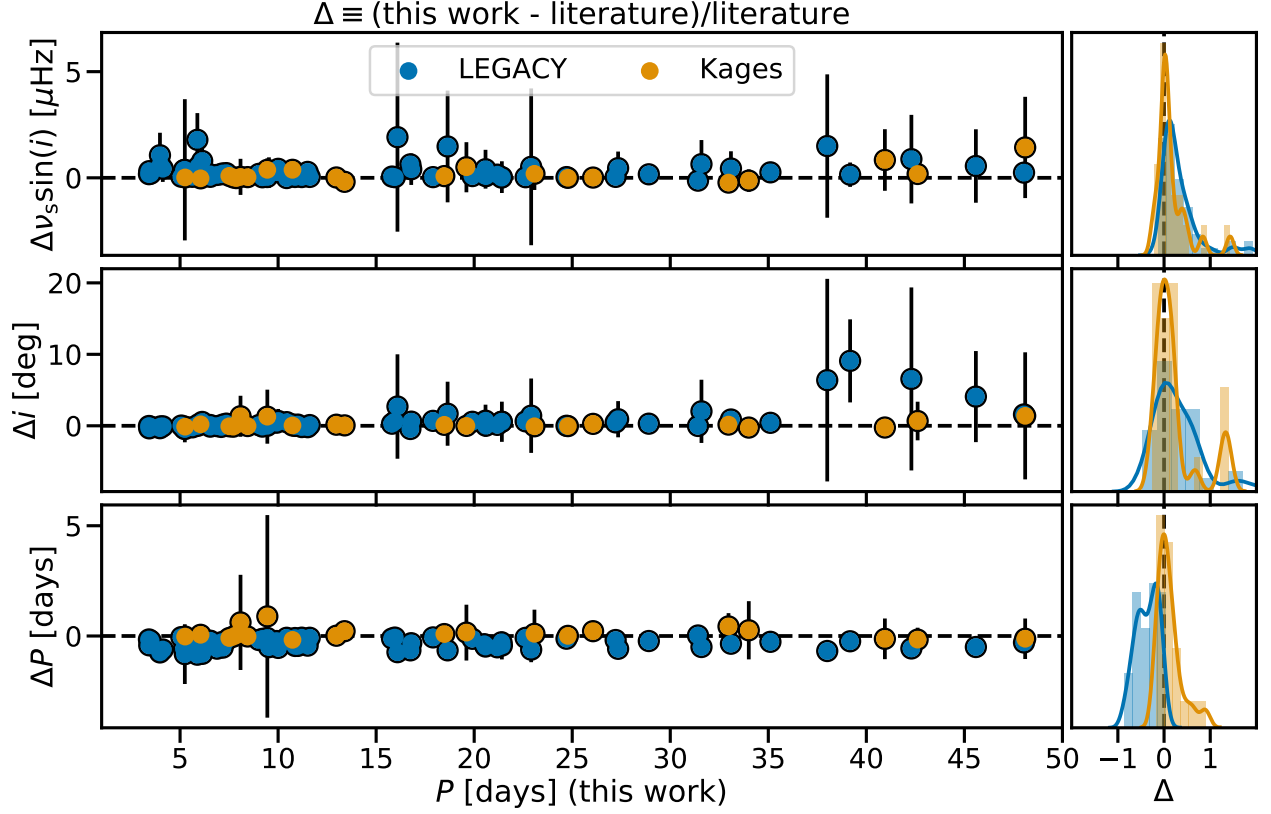


Figure 5: Comparisons between posterior estimates of rotational parameters from this work, LEGACY and Kages [22, 23, private communication]. Fractional differences are plotted against stellar rotation obtained in this work. The Δ indicates the fractional difference between this work and the literature (i.e. stars above the zero-line have higher values in this work). The right hand panels show the distribution of the fractional differences around the zero line. The colour legend is consistent throughout all panels. The x-axis units on the right hand panels are equivalent to the y-axis of the left hand panels. 10 stars have been omitted from this plot and are discussed in more detail in the text: KICs 5094751, 6196457, 8349582, 8494142, 8554498, 105114430 and 11133306 all have extremely low rotation periods in Kages, with high uncertainties. Conversely, KICs 6603624, 8760414 and 8938364 have extremely high rotation periods in LEGACY with low uncertainties. In cases where stars had asymmetric error bars, the larger of the two was used when propagating uncertainty for the purposes of this figure.

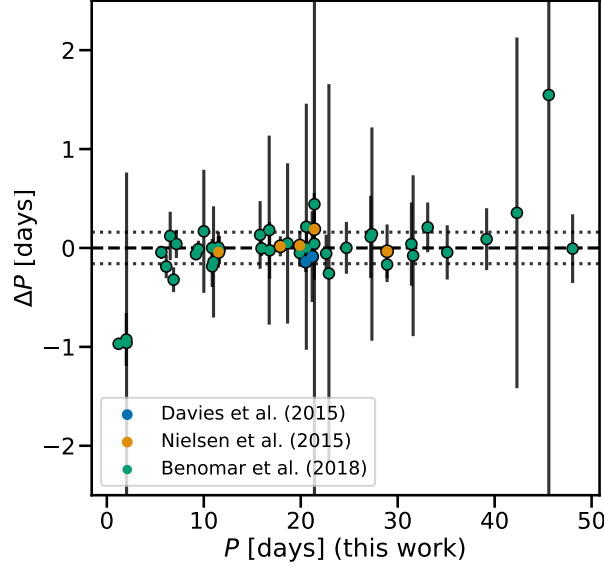


Figure 6: Fractional differences between posterior estimates of asteroseismic rotation period from this work. Literature sources are: [11] (16 Cyg A & B), [10] (5 stars) and [82] (40 stars). We used the reported parameter a_1 from [82], which represents the rotational splitting in the case of uniform latitudinal rotation in their model. The dashed line represents the median of the sample shown, with the dotted lines representing the 15.9th and 84.1st percentiles. In cases where stars had asymmetric error bars, the larger of the two was used when propagating uncertainty for the purposes of this figure.

of differential rotation with which our catalogue shares 40 targets. For the latter, we used their reported splitting value a_1 , which is equivalent to ν_s .

Overall, Figure 6 shows no strong disagreements between our asteroseismic measurements for stellar rotation and those from the literature. The scatter of the fractional differences lies cleanly around the zero line, with a mean and spread of $0.0^{+16.4}_{-15.6}$ %. The increase in uncertainty with period is due to more slowly rotating stars being more difficult to constrain using asteroseismology.

It is of note that 16 Cyg A, as reported by [11] was found to be rotating slightly faster in our analysis (deviating within 2σ), despite the fit being performed on the same data. We found an inclination angle that is slightly lower than [11] for 16 Cyg A but a similar projected splitting, which would explain finding a lower value of rotation.

There are three outliers at low period in Figure 6: KICs 6603624, 8760414 and 8938364. These are the same targets found to be outliers in a comparison to the LEGACY and Kages measurements (see above), with anomalously fast rotation rates and low inclination angles. As these stars represent the lowest inclination angles in our sample, and were found to disagree with two independent studies, we opted to exclude them from the gyrochronology analysis, and to flag the rotation measurements for these three stars presented in this work.

4.3 Internal vs external rotation

Different methods of rotation measurement probe different regions of stars. Asteroseismology of main sequence stars probes internal rotation in the near surface layers, where the observed p modes are most sensitive [20]. Measurements of star-spot modulation instead probe the rotation rates of star spots on the surface. A distinct difference between rotation rates obtained through these different techniques would hold information about differential rotation (both latitudinal and radial) of near-surface layers, such as those we observe in the Sun [83].

[10] performed a comparative analysis of 5 Sun-like stars observed with *Kepler* for which both star-spot modulation and asteroseismic rotation could be measured. They found no statistically significant difference between the two techniques.

Similarly, [21] performed an analysis on a larger sample of 22 stars. In this work they not only considered rotation rates from spots, but also spectroscopic measures of the projected surface rotation $v \sin(i)$, which they found to be more reliable. Comparisons with asteroseismic observations again showed no significant radial differential rotation.

With our expanded sample of asteroseismic rotation we can perform a similar analysis, to both validate our sample and probe radial differential rotation. Figure 7 shows a comparison between spectroscopic $v \sin(i)$ measurements as listed in LEGACY and Kages (left) and [21] (right). In these cases the asteroseismic $v \sin(i)$ has been calculated using our measure of asteroseismic $\nu_s \sin(i)$ and the known asteroseismic radii. Three stars (KICs 6603624, 8760414 and 8938364) have been excluded from this figure due to strong disagreements of measured rotation rates with the literature (see Section 4.2 above).

For the LEGACY and Kages sample, we find no strong deviation from the 1:1 line except at very low velocities, which is likely due to biases inherent to spectroscopic line broadening measurements [84, 85]. For the [21] sample stars lie a lot closer to the 1:1 line.

Overall, there appears to be a global offset where spectroscopic measurements of projected rotation appear faster than asteroseismic measures. Based on the LEGACY and Kages $v \sin(i)$ values, this offset is roughly 18% (i.e. spectroscopic projected rotation rates are higher than asteroseismic rates). This offset is much smaller ($\sim 5\%$) for the [21] sample, albeit for far fewer stars. These offsets are within the typical disagreement between spectroscopic methods, based on comparisons of projected rotation measurements for red giant stars [85, see Figure 2], especially at $< 5 \text{ km s}^{-1}$.

We also repeated the [10] comparison of asteroseismic rotation rates to surface rotation rates, using surface rotation measurements from [86] and [25]. Figure 8 shows comparisons for 48 stars with rotation rates from both techniques, including 4 from the original [10] sample. Rotation from spot-modulation are subject to measuring multiples of the true rotation rate, unlike an asteroseismic analysis [16], and therefore some stars may appear at the 2:1 and 1:2 lines on the Figure.

We repeated the analysis in [10] by fitting a line of the form $P_{\text{surf}} = m \times P_{\text{seis}}$. For the purposes of this fit we used the larger of the asymmetrical uncertainties on the seismic rotation from this work. In order to avoid biasing the fit due to outliers, we only included stars below the 1.8:1 line.

Our fit found a value of $m = 0.96 \pm 0.03$, showing a close agreement ($< 2\sigma$) between asteroseismic and surface rotation rates on a population level. Of the 40 stars that were

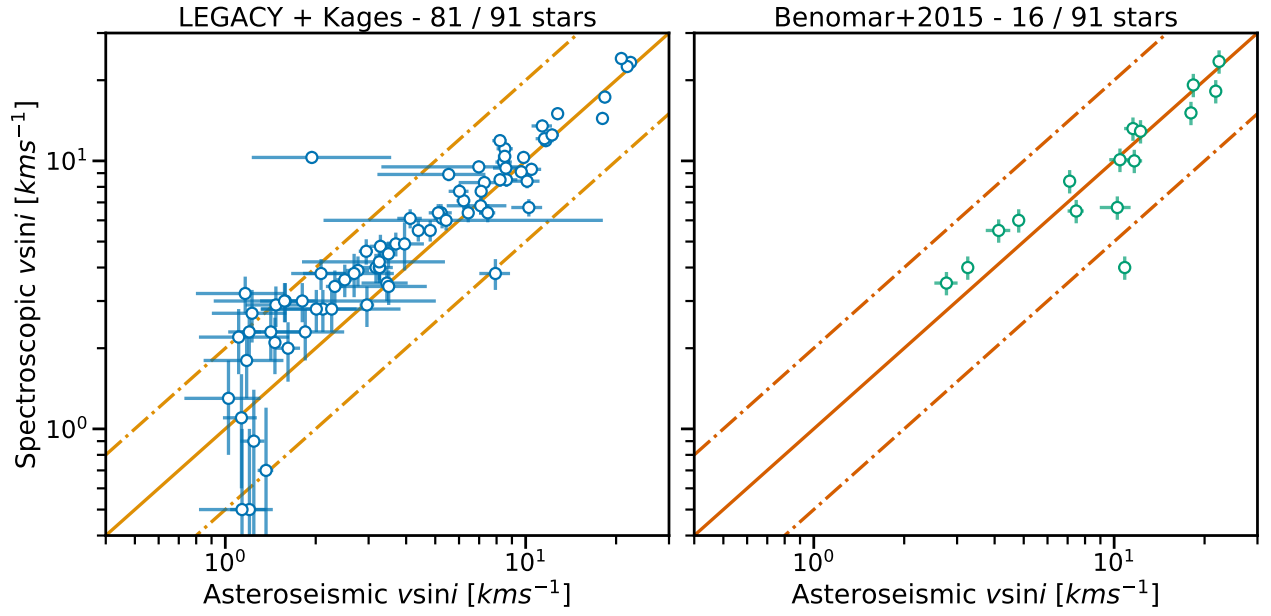


Figure 7: Comparisons between asteroseismic and spectroscopic measures of projected surface rotation, $v \sin(i)$. All asteroseismic (x-axis) values are from this work, all spectroscopic (y-axis) values are from the literature. *Left*: comparisons to 81 stars values reported in LEGACY and Kages. *Right*: comparisons to 16 stars observed by [21]. Asteroseismic values are transformed from projected splitting ($\nu_s \sin(i)$) using the asteroseismic radius measurements presented in LEGACY and Kages. The solid lines indicate the 1:1 line, while the dash-dotted lines represent the 2:1 and 1:2 lines.

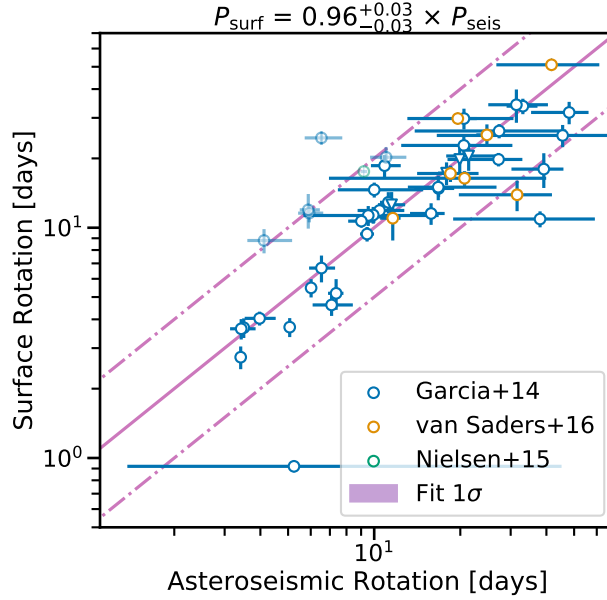


Figure 8: Comparisons between asteroseismic and photometric measures of stellar rotation, for 48 stars. Literature values were taken, in order of priority, from: [25] and [86] (i.e. if a value was reported in [86] and also in [25], the latter was used). Stars used in [2] are highlighted. The four triangles represent stars included in the original [10] work. The solid line indicates 1:1 line, while the dash-dotted lines represent 2:1 and 1:2 lines. The shaded region around the 1:1 line is the 1σ credible interval of the fit to the data, the result of which is shown as the title of the figure. Stars that were not included in the fitting process are transparent.

part of this analysis, 21 had a median value of $P_s < 0.5$ in the gyrochronology analysis. We repeated the model fit for these stars only, and found a value of $m = 0.96 \pm 0.04$. As we find no statistically significant deviation, we conclude that our asteroseismic ensemble is in agreement with surface rotation measurements of these stars, and can therefore be used to draw inferences about gyrochronology.

The overall agreement within the ensemble between the photometric measures of surface rotation and the asteroseismic rotation rates is in line with previous studies of Sun-like stars [87, 88, 10, 21], where different measures of rotation appear indistinguishable. Individual deviations from this agreement, as appears to be the case for a number of stars that lie distinctly off the bisector, may warrant a more in-depth analysis, which we leave to future work.

5 Verifying consequences for gyrochronology

5.1 Rotational models for different stellar types

Of the 73 stars for which posterior probability distributions of P_s were obtained, 4 were potential sub-giants, 22 were ‘hot’ stars, and 47 were main sequence stars. Different stellar types

should hold different amounts of diagnostic information about the standard or WMB models. Our ‘hot’ stars should hold little to no information, as they lie above the Kraft break, where traditional gyrochronology relations used to build the stellar models break down (specifically, they do not lose angular momentum with time). Similarly, the rotational evolution of sub-giant stars is dominated by envelope expansion, complicating the interpretation of rotation.

Figure ?? shows joint posterior distributions for P_s for the three different stellar types, as well as their cumulative distributions. Both the 4 sub-giant stars and the 22 ‘hot’ stars marginally prefer the standard model. The 47 MS stars on the other hand were most strongly in favour of weakened magnetic braking and dominate the full joint posterior. When only considering these stars, 99.2% of the joint probability fell below $P_s = 0.5$, compared to 98.4% for all 73 stars.

5.2 Limits of our stellar models

The models presented in [18] are constructed for metallicities of $-0.4 < [\text{Fe}/\text{H}] < 0.4$ dex, in steps of 0.1 dex. Our sample of 91 stars contained 4 stars with metallicities below -0.4 dex, which are shown as shaded symbols in Figure ?. Of these 4, 3 were included in our final sample of 73 stars used to evaluate our stellar models: KICs 7970740, 8684723 and KIC 9965715. All three are classed as MS stars, with metallicities of -0.54 ± 0.10 , -0.42 ± 0.10 and -0.44 ± 0.18 dex respectively, placing them within 3σ of the metallicity limits of our stellar models. KICs 8684723 and 9965715 strongly agree with the WMB model, whereas KIC 7970740 weakly prefers the standard model. Excluding these stars was not found to significantly alter the joint posterior distribution shown in Figure ?.

Recently, [89] compared different rotational evolution models [?,] of which we use the former in this work [vansaders+pinsonneault2013, matt+2015] while studying the effect metallicity has on rotation. They found that metal-rich stars spin down significantly more effectively than metal poor stars. The population of 73 stars used in our stellar model comparisons is roughly centered on a $[\text{Fe}/\text{H}]$ of 0 dex, with a spread of 0.16 dex, with no stars significantly above or below ± 0.4 dex (as discussed above). While differences in stellar rotational evolution as a function of metallicity in this region are still somewhat pronounced, they are much less so than for more metal-rich or poor stars [?, see Figure 2] amard+matt2020. However, for stars with $[\text{Fe}/\text{H}] < 0$, the [17] model prescription sees stars spin down more slowly than the models used in this work (i.e. they will rotate faster at later ages). This work only explores the presence of weakened magnetic braking for a single braking law, and a comparison to the [17] braking model will be explored in a future paper.

When constructing KDEs from our stellar model samples (see Section 2), we selected fixed resolutions (or band-widths) for the KDEs. In mass, the band-width of $0.02 M_\odot$, was larger than the uncertainties of 24 of 73 stars used to construct our joint posterior. For the stars with the smallest uncertainties, this significantly limits the size of the KDE being evaluated (as subsections of the full stellar models are used to evaluate individual stars, for computational efficiency). In order to confirm that these stars do not significantly affect the ensemble’s preference towards the WMB model, we recalculated the joint posterior distribution for P_s , excluding stars with an uncertainty on mass smaller than the KDE band-width. While the 24 stars with small uncertainties do favour the WMB model, they do so very weakly, whereas the remaining 49 stars with larger uncertainties strongly favour the WMB model. Their removal

from the total joint posterior probability does not significantly alter it from the distribution shown in Figure ??.

5.3 Systematic uncertainties from asteroseismology

In our model analysis, we used asteroseismic mass and age obtained using BASTA, as reported in LEGACY and Kages. Asteroseismic properties obtained through stellar models can be subject to systematic errors arising from differences in input physics and choice of stellar models not included in the reported statistical uncertainties. A quantification of these different systematic effects can be found in Section 4 of [8], based on the Kages catalogue. Combining their reported median systematic uncertainties due to input physics results in median uncertainties of 20% (up from 14%) on age and 5% (up from 3%) on mass for the Kages sample. For LEGACY, the median uncertainties are 18% (up from 10%) and 5.6% (up from 4%) for age and mass respectively.

In order to check the effect of systematic seismic uncertainties on our results for gyrochronology, we re-ran our model analysis described in Section 2 after inflating uncertainties on mass and age. We increased uncertainties by the fractional difference between the BASTA statistical uncertainties and the median full statistical and systematic uncertainties described above. For example, a LEGACY star with a mass of $2.0 \pm 0.5 M_{\odot}$ would have its uncertainty inflated by 1.6% of its mass, to $0.53 M_{\odot}$.

The results we found by repeating our model analysis with inflated uncertainties on asteroseismic mass and age closely replicated those found in our initial analysis. Specifically: subgiants preferred the standard model, and MS stars strongly favoured the WMB model. The ‘hot’ stars in this case slightly preferred the WMB model compared to the unaltered ensemble. The full joint posterior distribution for 73 stars still strongly favours of the WMB model even with the inflated uncertainties, including when considering only stars on the main sequence, when excluding stars outside the models’ metallicity range, and when excluding stars with low uncertainties on mass (see Section 5.2).

To further test the limits of this analysis, we reran our mixture model fit, this time only shifting the asteroseismic ages younger by the systematic uncertainty, and retaining the statistical uncertainty (i.e. the ages of LEGACY and Kages stars were reduced by 8% and 6% respectively). In this scenario where all asteroseismic ages are overestimated, ‘true’ fast rotators at young ages would have been mistaken for fast rotators at old ages, suggesting the presence of weakened magnetic braking where none existed. Despite the shift in age, the results from this mixture model fit closely matched those found for the unaltered ensemble, finding 95.8% of the total posterior probability to lie below $P_s = 0.5$ (as opposed to 98.4% for the unaltered ensemble). While the preference for the WMB model is slightly reduced, we conclude that the use of asteroseismic age is valid for the gyrochronology analyses presented in this work.

5.4 Binaries and Planet Hosts

For stars to be good probes of existing gyrochronology relations, their rotational evolution must occur in isolation. If a star interacts with a close binary companion (through tides, or

a merger) the natural angular momentum loss can be disturbed, causing gyrochronology to mispredict ages [4, 90]. Between LEGACY and Kages, we have 8 known binaries.

First, KIC 8379927, KIC 7510397, KIC 10454113 and KIC 9025370 are spectroscopic binaries. This does not affect the asteroseismic analysis, but may affect their rotational evolution. Of these, KICs 8379927, 7510397 and 9025370 were included in the gyrochronology analysis. None of them preferred one model strongly over the other, with all three finding flat posteriors for P_s .

Second, the binary pairs of KIC 9139151 & 9139163 and 16 Cyg A & B are individually observed binary components with wide orbital separations, so we do not expect their binarity to have affected their rotational evolution.

While we chose not to account for star-planet tidal interactions in this work, we note that this may also disturb the natural stellar rotational evolution when tidal forces are at play [91, 92, 93], although this has been disputed by observations of asteroseismic planet hosts [94].

5.5 Evidence for Weakened Magnetic Braking in the literature

Weakened magnetic braking was first proposed by [2], in response to stars with spot rotation rates faster than expected from gyrochronology at their asteroseismic ages. This discrepancy was also indicated at around the same time in other studies of asteroseismic ages of main sequence stars [10, 9, 11]. The theory of weakened magnetic braking has been both reinforced by recent studies [95], as well as disputed [96], at least at the critical Rossby number originally proposed.

As a sanity check that the evidence in favour of weakened magnetic braking presented in this work is independently robust, we recreated the joint posterior probability for P_s , this time looking only at MS stars, and excluding any of the 22 stars that were included in the original [2] sample. Of the 47 MS stars used to distinguish between stellar models, 16 were included in the [2] sample. Both the 16 [2] stars as well as the remaining MS stars favoured the WMB model, although the [2] stars did so more strongly, not including any stars that favoured the standard model. Specifically, when considering only the [2] stars, 96.3% of the total joint probability lay below $P_s = 0.5$, compared to 91.7% when considering only those stars *not* included in the [2] study. The stars initially used to propose the WMB model are still those most strongly in favour of it even when using asteroseismic rotation rates only.

Finally, we comment on the results found by [96]. Using spectroscopic rotation measurements of 14 solar twins, compared to grids of stellar models, they found marginal evidence favouring a standard rotational evolution. If weakened magnetic braking were to take place, it would most likely be outside the range of their sample, at $Ro_{\text{crit}} \geq 2.29$, compared to the value of 1.97 used in this work. Our sample does not overlap with theirs, so we can not directly compare to their results. However, our work does find statistical agreement between our asteroseismic rotation rates and ages, and a model of weakened magnetic braking at a critical Rossby number of 1.97. While a comparison to models of different Rossby numbers is outside the scope of this study, the LEGACY and Kages rotation sample may facilitate such studies in the future.